CONDENSED MATTER PHYSICS

Competing magnetic phases and fluctuation-driven scalar spin chirality in the kagome metal YMn_6Sn_6

Nirmal J. Ghimire[1,2]*, Rebecca L. Dally[3], L. Poudel[3,4], D. C. Jones[1,2], D. Michel[1,2], N. Thapa Magar[1], M. Bleuel[3,4], Michael A. McGuire[5], J. S. Jiang[6], J. F. Mitchell[6], Jeffrey W. Lynn[3], I. I. Mazin[1,2]

Identification, understanding, and manipulation of novel magnetic textures are essential for the discovery of new quantum materials for future spin-based electronic devices. In particular, materials that manifest a large response to external stimuli such as a magnetic field are subject to intense investigation. Here, we study the kagome-net magnet YMn_6Sn_6 by magnetometry, transport, and neutron diffraction measurements combined with first-principles calculations. We identify a number of nontrivial magnetic phases, explain their microscopic nature, and demonstrate that one of them hosts a large topological Hall effect (THE). We propose a previously unidentified fluctuation-driven mechanism, which leads to the THE at elevated temperatures. This interesting physics comes from parametrically frustrated interplanar exchange interactions that trigger strong magnetic fluctuations. Our results pave a path to chiral spin textures, promising for novel spintronics.

INTRODUCTION

Topologically nontrivial magnetic and electronic structures have attracted extraordinary attention in the past few years. Kagome-net magnets are one of the popular classes of these materials (*1*–*5*). It was recently realized that highly nontrivial physics can come from noncollinear interplanar ordering between ferromagnetic (FM) kagome planes, such as topological Hall effect (THE) in the absence of crystallographic inversion symmetry breaking (*6*, *7*). As opposed to anti-FM (AF) kagome materials, for FM kagome planes formed by the metals such as Fe or Mn, the in-plane exchange interaction is strongly FM and not magnetically frustrated but still forms characteristics of kagome geometry: Dirac cones, and flat bands (*8*–*12*). The interesting physics comes from the fact that, by virtue of the Mermin-Wagner theorem, the FM ordering in the two-dimensional planes is strongly suppressed, with the magnetic dynamics being controlled by weak interplanar exchange interactions, which, on the contrary, can be and usually are frustrated. Thus, these materials are strongly magnetically fluctuating and provide fertile ground for interesting new phenomena.

YMn_6Sn_6 is a prototype for this materials class. It forms a hexagonal *P6/mmm* structure ($a = 5.541$ Å and $c = 9.035$ Å) consisting of kagome planes [Mn_3Sn] separated by two inequivalent Sn_3 and Sn_2Y layers, i.e., [Mn_3Sn][Sn_3][Mn_3Sn][Sn_2Y] (Fig. 1, A and B) (*13*, *14*). YMn_6Sn_6 is a good metal (*15*, *16*), as can be seen in our resistivity data shown in Fig. 1C, and, hence, is expected to have relatively long-range exchange interactions, possibly including Ruderman-Kittel-Kasuya-Yosida coupling (Fig. 1A). All Mn planes and in-plane nearest-neighbor Mn—Mn bonds are crystallographically equivalent, but the interplanar Mn—Mn bonds along *c* are markedly different, with an FM exchange interaction across the Sn_3 layers and AF across the Sn_2Y layers. These are frustrated by the second-neighbor interaction across an intermediate Mn_3Sn layer (J_1 and J_3 are FM, while J_2 is AF) and result in complex magnetic behaviors (*14*, *15*). Below $T_N \approx 345$ K (Fig. 1D), a commensurate collinear AF structure first forms with the propagation vector $\mathbf{k} = (0, 0, 0.5)$. On cooling, an incommensurate phase quickly appears, which coexists with the commensurate phase in a narrow temperature range and becomes the only phase below 300 K (*14*, *17*). On the basis of powder diffraction, the incommensurate state has been reported to have two (and even three at room temperature) nearly equal wave vectors (*14*), which can be described as a staggered spiral, also dubbed the "double flat spiral," (*18*) as depicted in Fig. 1E. A magnetic field applied in the *ab* plane induces multiple transitions seen in the magnetization and Hall resistivity (*15*). An enigmatic THE is observed at elevated temperatures, with the largest value around 245 K and a magnetic field of 4 T (*16*). Here, we determine the microscopic origin of the magnetic field–induced phases of YMn_6Sn_6 and develop a theory describing the observed THE.

RESULTS AND DISCUSSION

We first present the different field-induced magnetic phases of YMn_6Sn_6 via bulk measurements. Figure 2A shows the magnetization measurements of YMn_6Sn_6 at two representative temperatures: 5 and 245 K. For the magnetic field applied along the *c* axis (red curve), the magnetization increases smoothly with field and, for 5 K, saturates slightly above 12 T, while the 245-K data show that the saturation field clearly decreases with increasing temperature. The effect of a magnetic field applied in the *ab* plane (H_{ab}) shown by the blue curves is more marked. At 5 K, we see a sharp increase at 2 T, indicative of a metamagnetic transition. A closer look reveals two close transitions, more apparent in the ac susceptibility measurement (Fig. 2B). Since the two transitions are very close, we denote the metamagnetic transition field by a single variable, H_1, for the remainder of the paper. As the field is further increased, the magnetization changes slope and increases continuously until $H_2 = 7$ T. Above H_2, the magnetization grows slower and saturates at $H_3 = 9.8$ T. As temperature is increased, H_1, H_2, and H_3 all shift to lower fields, and H_2 and H_3 become closer and merge. A phase diagram constructed from the ac susceptibility is depicted in Fig. 2B, with four main phases:

[1]Department of Physics and Astronomy, George Mason University, Fairfax, VA 22030, USA. [2]Quantum Science and Engineering Center, George Mason University, Fairfax, VA 22030, USA. [3]NIST Center for Neutron Research, National Institute of Standards and Technology, Gaithersburg, MD 20899, USA. [4]Department of Materials Science and Engineering, University of Maryland, College Park, MD 20742, USA. [5]Materials Science and Technology Division, Oak Ridge National Laboratory, Oak Ridge, TN 37831, USA. [6]Materials Science Division, Argonne National Laboratory, 9700 South Cass Avenue, Argonne, IL 60439, USA.
*Corresponding author. Email: nghimire@gmu.edu

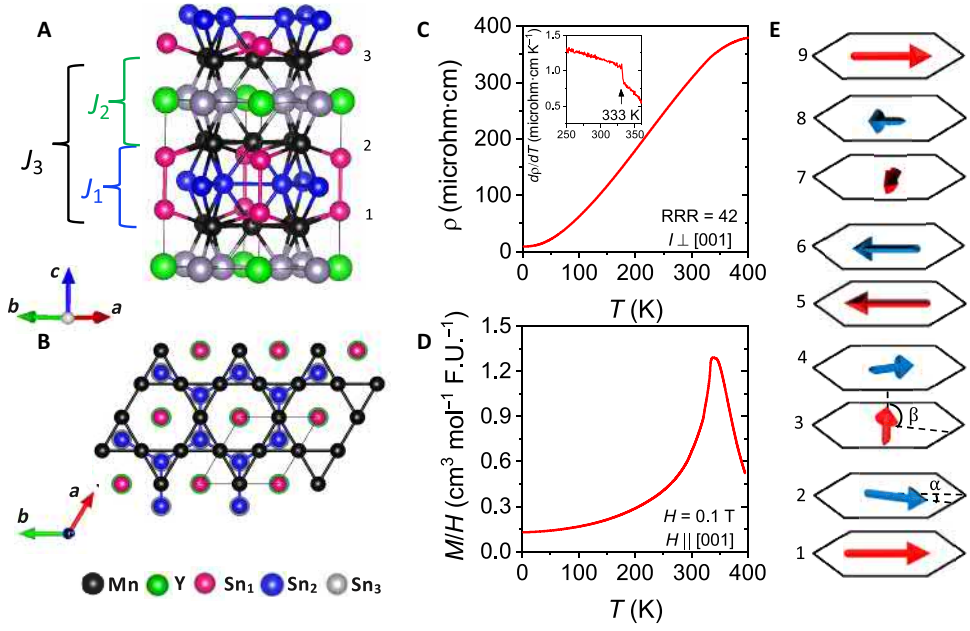

Fig. 1. Crystal structure and electrical and magnetic properties of YMn_6Sn_6. (**A**) Sketch of the crystal structure of YMn_6Sn_6. (**B**) Top view of the structure shown in (A). Within a unit cell shown by the grey solid lines, there are two kagome planes with the formula Mn_3Sn that are separated by Sn_3 and YSn_2 layers. The symbols J_i are the exchange constants between different Mn layers. (**C**) Electrical resistivity of YMn_6Sn_6 as a function of temperature with the electric current applied in the *ab* plane. Inset shows the temperature derivative of the electrical resistivity in the vicinity of T_N, which shows a jump at 333 K below which an incommensurate spiral state develops. The residual resistivity ratio (RRR = ρ_{400K}/ρ_{2K}) is 42 indicating a good sample quality. (**D**) Magnetic susceptibility (M/H) of YMn_6Sn_6 as a function of temperature. (**E**) Incommensurate magnetic structure of YMn_6Sn_6 in the absence of external magnetic field. Arrows represent the direction of FM spins within a kagome plane. There are small constant angles α between the FM-coupled spins across the Sn_3 layer, and β between the AF ones across the Sn_2Y, which result in a spiral spin arrangement, where every other Mn layer forms a spiral with the pitch defined by $\alpha + \beta \approx 90°$ and the two spirals rotated by α with respect to each other. The incommensurate spirals repeat after about four crystallographic unit cells or about nine Mn layers that are indicated by the numbers 1 to 9.

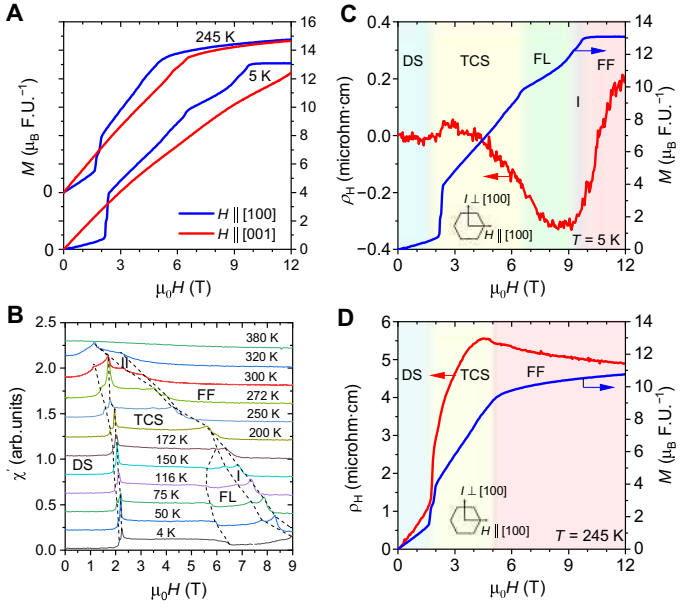

Fig. 2. Magnetization and Hall effect of YMn_6Sn_6. (**A**) Magnetization as a function of external magnetic field at 5 and 245 K with the magnetic field applied parallel and perpendicular to the *c* axis. Data have been offset as indicated. (**B**) Phase diagram of YMn_6Sn_6 constructed from ac susceptibility measurements. Arb. units, arbitrary units. (**C** and **D**) Hall resistivity (left axis) and magnetization (right axis) as a function of magnetic field applied in the *ab* plane at 5 K (C) and 245 K (D). The arrows in the hexagon in (C and D) indicate the filed and current direction in the basal plane of the hexagonal lattice of YMn_6Sn_6.

(i) $0 < H < H_1$, (ii) $H_1 < H < H_2$, (iii) $H_2 < H < H_3$, and (iv) $H > H_3$. We denote them as distorted spiral (DS), transverse conical spiral (TCS), fan-like (FL), and forced FM (FF), respectively, based on the magnetic structures as detailed below. The narrow intermediate phases between FL and FF and between TCS and FF are labeled "I" and "II," respectively.

The Hall resistivity (ρ_H) and magnetization (M) as a function of H_{ab} at 5 and 245 K are compared in Fig. 2 (C and D), respectively. At 5 K, ρ_H has a very small negative slope in the DS phase. At H_1, ρ_H shows a small jump but then decreases before increasing rapidly to saturation in the FF state, forming a remarkable minimum in the FL phase. The behavior of ρ_H is notably different at 245 K, where it exhibits a positive slope in the DS phase. At the metamagnetic transition (H_1), it shows a sizable jump and then increases nonlinearly with the magnetization in the TCS phase, which has been interpreted as the THE (*16*).

The zero-field neutron diffraction data are plotted in Fig. 3A. A commensurate magnetic Bragg peak is observed at the onset of long-range magnetic order, where $\mathbf{k} = (0, 0, 0.5)$ and $T_N = 345$ K, which quickly transforms into two distinct incommensurate wave vectors. These two incommensurate structures coexist from their onset to the base temperature (12 K) determined by high-resolution measurements (inset in Fig. 3A). The two wave vectors $(0, 0, k_{z,1})$ and $(0, 0, k_{z,2})$ with $k_{z,1} < k_{z,2}$ evolve smoothly with temperature along L, and $|k_{z,1} - k_{z,2}|$ decreases with cooling. The two magnetic structures stemming from $k_{z,1}$ and $k_{z,2}$ are consistent with previous reports (*14*, *18*) (see Fig. 1E) but with slightly different periodicities (fig. S4A).

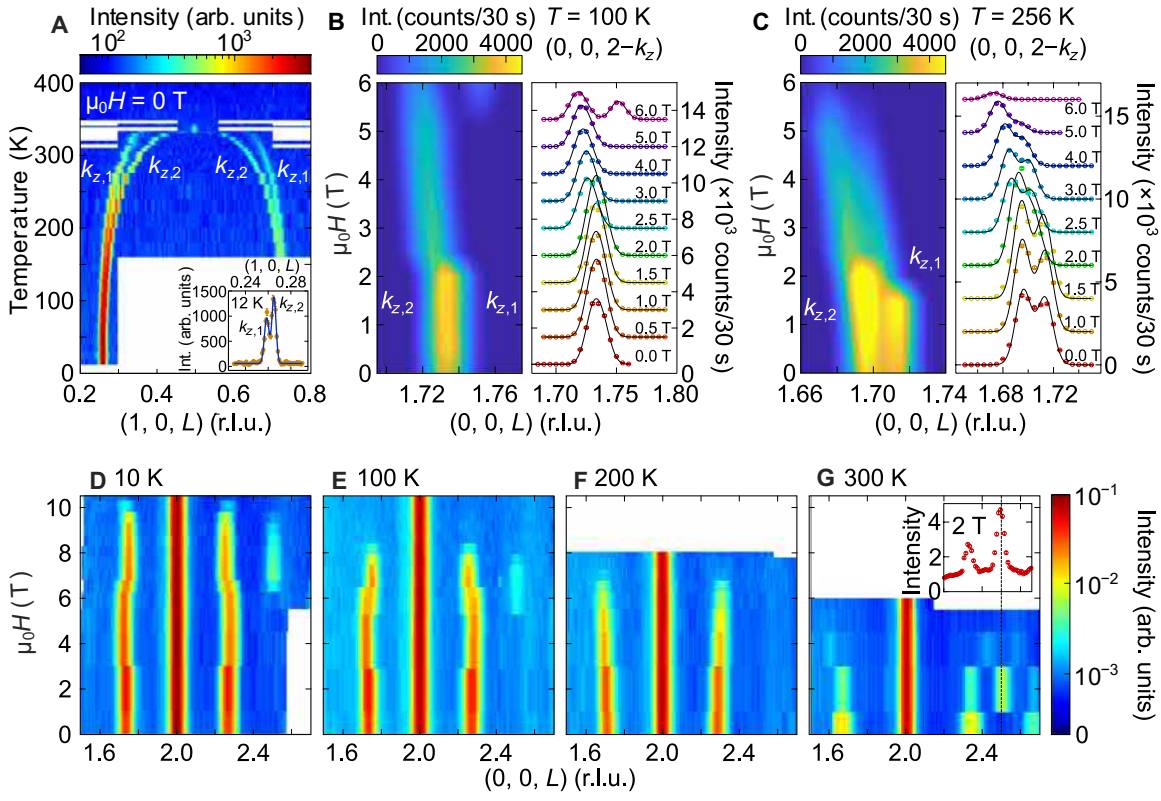

Fig. 3. Single-crystal neutron diffraction of YMn_6Sn_6. (**A**) Magnetic Bragg peaks tracked as a function of temperature. A commensurate magnetic peak at L = 0.5 appears between 345 and 330 K, and the two incommensurate magnetic structures stemming from the wave vectors $k_{z,1}$ and $k_{z,2}$ appear at 330 K and persist to the base temperature measured (12 K). The inset, taken with high instrumental resolution, shows that the two wave vectors do not converge, even as they get closer with decreasing temperature. (**B** and **C**) Incommensurate magnetic Bragg peaks (0, 0, 2 − $k_{z,n}$) (n = 1,2) tracked at 100 and 256 K, respectively, as a function of applied magnetic field. The solid black lines in the right-hand panels of (B) and (C) are Gaussian fits to the data described in Materials and Methods. An offset was added between individual L scans for clarity. Offsets are 1500 counts/30 s for (B) and 2000 counts/30 s for (C). (**D** to **G**) Neutron diffraction data taken up to higher fields with a position sensitive detector and coarse resolution for (D) 10 K, (E) 100 K, (F) 200 K, and (G) 300 K. In these data, $k_{z,1}$ and $k_{z,2}$ are not resolvable, but the high fields at which the data were taken reveal the field ranges at which each of the magnetic phases are present. The inset of (G) is a cut taken from the main panel at 2 T, where the dashed black line shows that the new peak appearing at this field is commensurate at L = 2.5.

We now focus on the multiple magnetic phases induced via application of an external magnetic field in the *ab* plane. Figure 3 (B and C) shows data taken about (0, 0, 2 − $k_{z,n}$) (n = 1, 2) for 100 and 256 K, respectively. We find that $k_{z,n}$ are almost field independent, except for an abrupt shift to larger momentum for both magnetic peaks at H_1, which lies between 2.0 and 2.5 T (between 1.5 and 2.0 T for H_1 at 256 K). Concomitant with these shifts are pronounced decreases in intensity of the Bragg peaks at (0, 0, $L \pm k_{z,n}$) positions. The T = 100 K data show a new commensurate structure emerging at H_2 (6 T), with the wave vector (0, 0, k_c), where k_c = 0.25 and a satellite at 2k_c-type positions, which can be seen in Fig. 3E (discussed more below). These commensurate peaks coexist with the incommensurate peaks at 6 T and emerge at the cost of the incommensurate intensities (see section S2 for details).

A 15-T magnet was used to focus on the high-field behavior, where coarse instrumental resolution was used to compensate for the reduced intensities. The two incommensurate wave vectors are not resolvable with this resolution, but the data satisfactorily capture the overall high-field behavior. Figure 3F shows that, at 200 K, the incommensurate peaks disappear above 7 T, similar to the observation that they are almost fully suppressed by 6 T in the 256-K high-resolution data (Fig. 3C). The **k** = (0, 0, 0.25) commensurate structure at 100 K and 6 T in Fig. 3B can be seen at the same field in Fig. 3E at **Q** = (0, 0, 2.25) with a satellite peak at **Q** = (0, 0, 2.50). In addition, we see that all but the FF structures disappear above 8 T as the spins become fully polarized. The high-field commensurate phase persists down to 10 K, shown in Fig. 3D, but is shifted higher in field and is present between 6.5 and 9.5 T.

The neutron data capture all the features observed in bulk magnetic measurements (Fig. 2). Below H_1, there is very little change to the incommensurate peaks. At H_1, the wave vector positions change by ~3%, and intensity drops as much as 60% (see fig. S4). The H_1 transition, which spans almost the entire temperature range of zero-field incommensurability, resembles a spin-flop transition, deduced from the magnetization data in Fig. 2A. As discussed further in the theoretical section, this is a spin flop from a helical to cycloidal spiral. Comparison of the structure factor calculations for each magnetic structure to the data supports this assignment (see section S2 and fig. S5 for details). At H_2, commensurate peaks with **k** = (0, 0, 0.25)–type positions, as well as satellites at 2k_c, emerge at the cost of the incommensurate structures. The commensurate peaks only appear in the FL phase. Curiously, however, a commensurate phase with propagation vector **k** = (0, 0, 0.5) is seen to emerge at 300 K and low field (2 T) as seen in Fig. 3G. This temperature and field reside within region II of the phase diagram in Fig. 2B.

To understand the microscopic origin and nature of the different magnetic phases, we performed first-principles density functional theory (DFT) calculations and used the results to construct a mean field theory at $T = 0$. The details are presented in Materials and Methods and section S3, and here, we summarize the main findings. First, DFT total energy calculations were performed and fit to the Hamiltonian (Eq. 1)

$$\mathcal{H} = \sum_{i,j} J_n \mathbf{n}_i \cdot \mathbf{n}_j + \sum_{i,j} J_p \mathbf{n}_i \cdot \mathbf{n}_j + K \sum_i \left(n_i^z\right)^2 + \sum_i J^z n_i^z \cdot n_{i+1}^z + \sum_i \mathbf{n}_i \cdot \mathbf{H} \quad (1)$$

where $\mathbf{H}$ is the external field and $\mathbf{n}$ is a unit vector along the local magnetization direction. The first sum runs over six nearest neighbors along the c axis, the second sum runs over the first neighbors in the ab plane, and the last three sums run over all atoms ($i + 1$ denotes the nearest c-axis neighbor). K is the easy-plane single-ion anisotropy, and the Ising-type anisotropic exchange, J^z, is the only one allowed by symmetry for the vertical bonds. To account for Hubbard correlations, we added a DFT + U correction (see section S3). We found that the best description of the ground state is attained for $U - J = 0.4$ to 0.6 eV, and in the following, we use 0.4 eV (not unreasonable for a good metal). The results are shown in the table S2 for three models: "full," "reduced," where J_{4-6} are absorbed into modified J_{2-3}, and "minimal," where J_z is, in addition, combined with K. The full model has a staggered spiral as a ground state, as shown in Fig. 1E, with the two angles $\alpha = -22°$ and $\beta = 138°$, in reasonable agreement with the low-temperature experimental $\mathbf{k} \approx (0, 0, 0.25)$ described by the pitching angles $\alpha = -20°$ and $\beta = 110°$ ($\alpha + \beta = 90°$). These angles were used in the reduced model, J_{2-3}, calculations.

We now present the mean field theory results for the minimal and reduced models at $T = 0$. At $H = 0$, one gets a staggered spiral (*14*). Without K, the minimal model uniquely defines (*14*) the propagation vector k_z but is degenerate with respect to the plane in which the magnetic moments rotate. The anisotropy K locks the spins to the ab plane. Results for the mean field theory are shown in Fig. 4 (A to C) (see section S4 for details). The behavior for $H \| c$ is trivial: The helical spiral becomes a longitudinal conical spiral (LCS) and gradually transforms into a field-polarized FM phase. For $H \| a$, if there were no magnetic anisotropy ($K = 0$), then the staggered spiral would immediately flop from spins rotating in the ab plane (helical) to those rotating in the bc plane (cycloidal), which would then gradually cant into a TCS state, and eventually saturate. The magnetic anisotropy sets a finite spin-flop field $H_1 \propto \sqrt{\langle J \rangle K}$, where $\langle J \rangle$ is the appropriately averaged J_{1-3} parameters. Below H_1, the spiral remains flat but distorts slightly by canting each spin a little toward a (this is the DS phase). At H_1, the magnetization increases discontinuously. However, when the conical angle in the TCS phase above H_1 becomes rather small, at the field H_2, not that far from the saturation field, further canting gains too little energy, and it becomes energetically favorable to flop back into the ab plane, gaining back some of the anisotropy energy. The resulting phase, found by minimization of the minimal Hamiltonian, is a very unusual commensurate FL phase, depicted in Fig. 4B. It can be described as a quadrupled structure along the c axis, with spins deviating from the x direction, the direction of the magnetic field, by the angles $\gamma, \gamma, -\delta, \delta, -\gamma, -\gamma, \delta, -\delta$, which gradually decrease until the FF state, $\gamma = \delta = 0$, is reached (see section S4 for details). The FL phase has a different periodicity for M_x, the projection of Mn moments onto the x axis, and for M_y, the projection onto the perpendicular in-plane axis. The latter corresponds to $k_c = 0.25$, the former to $k_c = 0.5$, and the variation of amplitude of M_x is much smaller. The calculations (Fig. 4C) capture all features of the measured magnetization (Fig. 2A). The predictions are also confirmed by our neutron data: The first spin flop from a nearly helical to a nearly cycloidal spiral leads to about 50% loss in the scattering intensity for $(0, 0, L \pm k_{n,z})$–type Bragg peaks (neutrons do not scatter off the M_z component in our geometry when the scattering vector is along L), consistent with the discontinuous loss of intensity in the experiment (see section S2). In the minimal model, the first spin flop does not alter the periodicity; experimentally, however, k_z slightly increases in the TCS phase. To understand this, we need to step back to the reduced model that retains separation of K and J^z. Then, the mean field theory predicts a tiny shortening of the spiral pitch at $H = H_1$, on the scale of $\approx 0.36 J^z/J_1 \sim 1\%$ (see section S4). The FL phase also finds full confirmation in the experiment: At $H = H_2$, as predicted, k_z changes discontinuously to $k_c = 0.25$, and the predicted weaker satellite at $2k_c$ is observed as well.

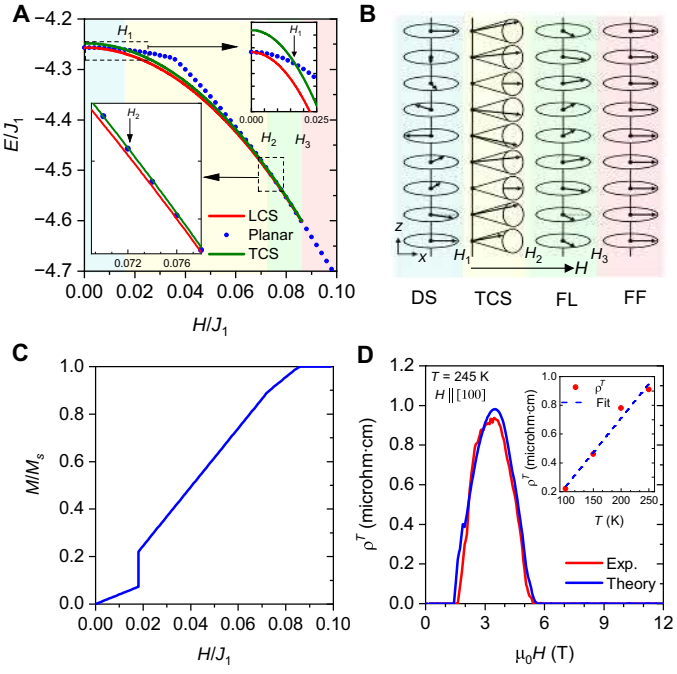

Fig. 4. First-principles calculation and phenomenological model of spin chirality for THE. (**A**) Energy for different magnetic states as a function of reduced magnetic field obtained in mean field calculations. The planar state represented by the blue dotted line has DS structure below the kink and FL structure above the kink. (**B**) Sketch of different field-induced magnetic structures. (**C**) Calculated magnetization as a function of in-plane field. (**D**) Experimental and theoretical topological Hall resistivity given by Eq. 2 as a function of external magnetic field at 245 K. Inset shows the temperature variation of the THE at 4 T below 250 K. The dashed line is a linear fit to the experimental data.

We now focus on the THE and show its origin in a fluctuation-driven chirality. The THE appears in the TCS phase only. The fact that the THE is observed only at elevated temperatures, while the TCS phase exists in the entire temperature range below 330 K, strongly suggests the key role of thermal fluctuations. It is worth remembering that the system is strongly two-dimensional, with nearly two orders of magnitude difference between the ab and c couplings. In this case, by virtue of the Mermin-Wagner theorem, the mean field transition

temperature of several thousand kelvin is markedly suppressed by large and relatively slow in-plane fluctuations. This is reminiscent of the famous nematic transition in the planar $J_1 - J_2$ Heisenberg mode (*19*), where these fluctuations can give rise to a new, nonmagnetic order parameter without a long-range magnetic order. This so-called nematic phase is realized in many Fe-based superconductors (*20*) and maybe in other materials as well (*21*).

We will argue now that similar physics may be realized in the TCS phase. The detailed theory is provided in section S5. Here, we present a summary of the results. In a continuous approximation, the TCS can be described as $\mathbf{M} = \mathbf{M}_x + \mathbf{m}$, where $\mathbf{M}_x \,||\, \hat{\mathbf{x}}$ is the induced magnetic moment and is a constant, and $\mathbf{m} \perp \hat{\mathbf{x}}$ is a cycloidal spiral. It is also assumed that while the direction of the Mn moment can change and fluctuate, the amplitude stays the same. The topological chiral field given by the standard expression (*2*) $b_x = \mathbf{M} \cdot (\partial_y \mathbf{M} \times \partial_z \mathbf{M}) = \partial_y \mathbf{M} \cdot (\partial_z \mathbf{M} \times \mathbf{M})$ is thus zero in the TCS phase (or in any phase) where $\partial_y \mathbf{M} = \mathbf{0}$, and hence, there is no THE. However, addition of a magnon fluctuation, propagating along y with wave vector k_y, gives $\mathbf{M} = M_x\mathbf{x} + \mathbf{m} + \boldsymbol{\mu}$ where, as mentioned, $\mathbf{m} \perp \mathbf{x}$ and $\boldsymbol{\mu}$ represents a magnon propagating along y (to have nonzero $\partial_y \mathbf{M}$) in a plane defined by a vector $\boldsymbol{\omega}$, such that $\boldsymbol{\omega} \propto k_y$. Then, $\frac{\partial \mathbf{M}}{\partial z} = \frac{\partial \mathbf{m}}{\partial z} = \mathbf{m} \times \hat{\mathbf{x}}$, and $\frac{\partial \mathbf{M}}{\partial y} = \frac{\partial \boldsymbol{\mu}}{\partial y} = \boldsymbol{\mu} \times \boldsymbol{\omega}$. Using these equations on b_x, keeping only the terms quadratic in $\boldsymbol{\mu}$ and averaging over y, gives $b_x = -k_y m_z \mu^2$, and, unless $\boldsymbol{\omega} \,||\, \hat{\mathbf{x}}$, $b_x \neq 0$.

The physical meaning of this result is very simple; the TCS is one independent magnon short of a chiral combination of static magnons. Of all possible magnons, there are some that generate positive chirality, but, by crystallographic symmetry, for each such magnon, there is a partner with the same energy and opposite chirality. These two partners will be thermally excited with the same probability, and their effect will cancel each other, in the absence of an external field. However, in an applied field, they create nonzero chiral susceptibility, reminiscent of the nematic susceptibility in Fe-based superconductors. We find the chiral field in such a case to be

$$\langle b_x \rangle = \text{const} \cdot TM_z^2 H_x = \text{const} \cdot \left(1 - M^2/M_s^2\right) TH_x \qquad (2)$$

The topological Hall resistivity (ρ^T) is proportional to $\langle b_x \rangle$, and hence, ρ^T can be calculated by Eq. 2 using experimental parameters. Note that this expression is valid only for $H_1 < H_x < H_2$ and the topological Hall resistivity is zero outside these limits. The theoretical ρ^T is plotted together with the measured data at $T = 245$ K in Fig. 4D. The inset shows the temperature dependence of ρ^T at a constant field of 4 T, which is linear in temperature as expected from Eq. 2 (M_z depends on the temperature very weakly, as one can see from the experimental data in fig. S17). The details of the experimental and theoretical ρ^T are provided in the section S6. The remarkable agreement of the experimental data with this phenomenological model provides insight into the microscopic origin of the THE as stabilized by the thermal fluctuations, creating an imbalance in the right- and left-handed TCSs, a nematic spin chirality. We want to point out that the exceptional agreement between theory and experimental THE may be, to some extent, fortuitous, given the simplicity of the model and partitioning of the total ρ_H (discussed in detail in section S6), but provides strong support to the presented physical picture, describing the observed THE. Note that quantization of the Hall effect has been discussed in two-dimensional kagome-lattice ferromagnets (*22*), where the spin tilting provides the necessary scalar chirality. The mechanism we propose here, however, is different since the observed chiral response arises from preferentially exciting spin fluctuations propagating in one direction (at the expense of those moving in the opposite direction) within a particular spiral state.

We have identified two unique magnetic phases, TCS and FL, in YMn_6Sn_6, which emerge from the competitions between exchange interactions, the magnetic anisotropies, and Zeeman energy, with a remarkable agreement between bulk measurements, neutron diffraction, and first-principles calculations. The THE in the TCS phase is of particular interest. As opposed to noncoplanar and skyrmionic materials, this spiral magnet without static spin chirality forms a nonzero internal skyrmionic magnetic field dynamically, through preferential excitation of chiral fluctuations with a given handedness. This field deflects the conducting charge and thus produces the extra component to the Hall effect, the THE. Our results not only provide a new mechanism for the THE but also open promising avenues in looking for chiral spin fluctuations in new materials and at temperatures relevant for practical applications. Moreover, it is well known that spin-orbit coupling in kagome-lattice magnets can mediate the entanglement of the electronic and magnetic topology giving rise to more exotic correlated phenomena (*12*, *23*). Recently, a novel electronic topological phenomenon has been realized in the isostructural compound $TbMn_6Sn_6$ (*24*). Thus, this family of compounds may provide prototypes to study the interplay of topological properties simultaneously arising both in real and momentum space.

MATERIALS AND METHODS

Crystal growth and characterization

Single crystals of YMn_6Sn_6 were grown by the self-flux method. Y pieces (Alfa Aesar; 99.9%), Mn pieces (Alfa Aesar; 99.95%), and Sn shots (Alfa Aesar; 99.999%) were loaded in a 2-ml aluminum oxide crucible in a molar ratio of 1:1:20. The crucible was then sealed in a fused silica ampoule under vacuum. The sealed ampoule was heated to 1175°C over 10 hours, homogenized at 1175°C for 12 hours, and then cooled to 600°C over 100 hours. Once the furnace reached 600°C, the excess flux was decanted from the crystals using a centrifuge. Well-faceted hexagonal crystals as large as 100 mg were obtained. The crystal structure of the compound was verified by x-ray powder diffraction at room temperature using a Rigaku MiniFlex diffractometer. A few crystals from each growth batch were ground into powder, and x-ray diffraction patterns were collected on those powder samples. Rietveld refinement (*25*) of a representative powder x-ray pattern using FullProf software (*26*) is shown in fig. S1. Magnetic and transport measurements were carried out on oriented single crystals.

Magnetic and transport property measurements

dc susceptibility measurements were made using a Quantum Design VSM SQUID. dc magnetization and transport measurements were measured using a physical property measurement system (PPMS). ac susceptibility measurements were carried out using a Quantum Design DynaCool PPMS. Resistivity and Hall measurements were performed following the conventional 4-probe method. Pt wires of 25 μm in diameter were attached to the sample with EPO-TEK H20E silver epoxy. An electric current of 1 mA was used for the transport measurements. In magnetoresistance measurements, the contact misalignment was corrected by field symmetrizing the measured data.

Neutron diffraction measurements

A single crystal was oriented in either the $(H, 0, L)$ or (H, H, L) scattering plane on the triple-axis neutron spectrometer BT-7 (*27*) at the National Institute of Standards and Technology Center for Neutron Research. Elastic diffraction data were taken with $E_i = E_f = 14.7$ meV and 25′ – 10′ – 10′ – 25′ full width at half maximum (FWHM) collimators were used before and after the sample, before the analyzer, and before the detector, respectively (unless otherwise noted). A superconducting 7-T vertical field magnet system with a top-loading closed cycle refrigerator was used at the sample position such that the applied field was parallel to the [1, $\bar{1}$, 0] crystallographic direction. Bragg peaks were resolution limited and Gaussian in shape. Peaks were therefore fit to Gaussians with the FWHMs constrained to be that of the spectrometer resolution as determined by the program ResLib (*28*). Data using a superconducting 15-T vertical field magnet system were taken in the (H, H, L) scattering plane, where the magnetic field was also parallel to [1, $\bar{1}$, 0]. Moderately coarse resolution was used with open –50′ – 40′R – 120′ collimators (where "R" indicates radial) and a position-sensitive detector. Throughout the manuscript, momentum is reported in reciprocal lattice units (r.l.u.) denoted using H, K, and L, where $\mathbf{Q}\,[\text{Å}^{-1}] = \left(\frac{4\pi}{\sqrt{3}\,a}H, \frac{4\pi}{\sqrt{3}\,a}K, \frac{2\pi}{c}L\right)$.

First-principles calculations

Most calculations were performed using the projected augmented wave pseudo-potential code VASP (*29*) and the gradient-dependent density functional of (*30*). For control purposes, some calculations were also repeated using the all-electron linearized augmented plane wave code WIEN2k (*31*). Hubbard correlations were taking into account using the DFT + U with the fully localized double counting prescription and the spherically averaged correction $U - J$, with the values of $U - J$ given in Results and Discussion section.

SUPPLEMENTARY MATERIALS

Supplementary material for this article is available at http://advances.sciencemag.org/cgi/content/full/6/51/eabe2680/DC1

REFERENCES AND NOTES

1. J. Zang, V. Cros, A. Hoffmann, *Topology in Magnetism* (Springer, 2018).
2. N. Nagaosa, Y. Tokura, Topological properties and dynamics of magnetic skyrmions. *Nat. Nanotechnol.* **8**, 899–911 (2013).
3. N. Nagaosa, X. Z. Yu, Y. Tokura, Gauge fields in real and momentum spaces in magnets: Monopoles and skyrmions. *Phil. Trans. R. Soc. A* **370**, 5806–5819 (2012).
4. B. Bradlyn, J. Cano, Z. Wang, M. G. Vergniory, C. Felser, R. J. Cava, B. A. Bernevig, Beyond Dirac and Weyl fermions: Unconventional quasiparticles in conventional crystals. *Science* **353**, aaf5037 (2016).
5. N. P. Armitage, E. J. Mele, A. Vishwanath, Weyl and Dirac semimetals in three-dimensional solids. *Rev. Mod. Phys.* **90**, 15001 (2018).
6. J. Kübler, C. Fesler, Non-collinear antiferromagnets and the anomalous Hall effect. *Europhys. Lett.* **108**, 67001 (2014).
7. S. Nakatsuji, N. Kiyohara, T. Higo, Large anomalous Hall effect in a non-collinear antiferromagnet at room temperature. *Nature* **527**, 212–215 (2015).
8. N. J. Ghimire, I. I. Mazin, Topology and correlations on the kagome lattice. *Nat. Mater.* **19**, 137–138 (2020).
9. M. Kang, L. Ye, S. Fang, J.-S. You, A. Levitan, M. Han, J. I. Facio, C. Jozwiak, A. Bostwick, E. Rotenberg, M. K. Chan, R. D. Mc Donald, D. Graf, K. Kaznatcheev, E. Vescovo, D. C. Bell, E. Kaxiras, J. van den Brink, M. Richter, M. P. Ghimire, J. G. Checkelsky, R. Comin, Dirac fermions and flat bands in the ideal kagome metal FeSn. *Nat. Mater.* **19**, 163–169 (2020).
10. L. Ye, M. Kang, J. Liu, F. von Cube, C. R. Wicker, T. Suzuki, C. Jozwiak, A. Bostwick, E. Rotenberg, D. C. Bell, L. Fu, R. Comin, J. G. Checkelsky, Massive Dirac fermions in a ferromagnetic kagome metal. *Nature* **555**, 638–642 (2018).
11. E. Liu, Y. Sun, N. Kumar, L. Muechler, A. Sun, L. Jiao, S.-Y. Yang, D. Liu, A. Liang, Q. Xu, J. Kroder, V. Süß, H. Borrmann, C. Shekhar, Z. Wang, C. Xi, W. Wang, W. Schnelle, S. Wirth, Y. Chen, S. T. B. Goennenwein, C. Felser, Giant anomalous Hall effect in a ferromagnetic kagome-lattice semimetal. *Nat. Phys.* **14**, 1125–1131 (2018).
12. J. X. Yin, S. S. Zhang, G. Chang, Q. Wang, S. S. Tsirkin, Z. Guguchia, B. Lian, H. Zhou, K. Jiang, I. Belopolski, N. Shumiya, D. Multer, M. Litskevich, T. A. Cochran, H. Lin, Z. Wang, T. Neupert, S. Jia, H. Lei, M. Z. Hasan, Negative flat band magnetism in a spin–orbit-coupled correlated kagome magnet. *Nat. Phys.* **15**, 443–448 (2019).
13. C. Lefèvre, A. Verniere, G. Venturini, B. Malaman, A neutron diffraction study of $HfFe_6Ge_6$-type $YMn_6Sn_{6-x}In_x$ compounds ($0.03 \leq x \leq 0.72$). *J. Alloys Compd.* **361**, 40–47 (2003).
14. G. Venturini, D. Fruchart, B. Malaman, Incommensurate magnetic structures of RMn_6Sn_6(R = Sc, Y, Lu) compounds from neutron diffraction study. *J. Alloys Compd.* **236**, 102–110 (1996).
15. K. Uhlíová, F. R. deoer, V. Sechovský, G. Venturini, Magnetism of YMn_6Sn_6 and $DyMn_6Ge_6$: Single-crystal study, in *WDS'06 Proceedings of Contributed Papers Part III* (Matfyzpress, 2006), pp. 48–53.
16. Q. Wang, Q. Yin, S. Fujitsu, H. Hosono, H. Lei, Near-room-temperature giant topological Hall effect in antiferromagnetic kagome metal YMn_6Sn_6. arXiv: 1906.07986 [cond-mat. str-el] (19 June 2019).
17. H. Zhang, X. Feng, T. Heitmann, A. I. Kolesnikov, M. B. Stone, Y.-M. Lu, X. Ke, Topological magnon bands in a room-temperature kagome magnet. *Phys. Rev. B* **101**, 100405 (2020).
18. E. V. Rosenfeld, N. V. Mushnikov, Double-flat-spiral magnetic structures: Theory and application to the compounds. *Physica B* **403**, 1898–1906 (2008).
19. P. Chandra, P. Coleman, A. I. Larkin, Ising transition in frustrated Heisenberg models. *Phys. Rev. Lett.* **64**, 88–91 (1990).
20. R. M. Fernandes, A. V. Chubukov, J. Schmalian, What drives nematic order in iron-based superconductors? *Nat. Phys.* **10**, 97–104 (2014).
21. G. Zhang, J. K. Glasbrenner, R. Flint, I. I. Mazin, R. M. Fernandes, Double-stage nematic bond ordering above double stripe magnetism: Application to $BaTi_2Sb_2O$. *Phys. Rev. B* **95**, 174402 (2017).
22. K. Ohgushi, S. Murakami, N. Nagaosa, Spin anisotropy and quantum Hall effect in the *kagomé* lattice: Chiral spin state based on a ferromagnet. *Phys. Rev. B* **62**, R6065–R6068 (2000).
23. K. Kuroda, T. Tomita, M.-T. Suzuki, C. Bareille, A. A. Nugroho, P. Goswami, M. Ochi, M. Ikhlas, M. Nakayama, S. Akebi, R. Noguchi, R. Ishii, N. Inami, K. Ono, H. Kumigashira, A. Varykhalov, T. Muro, T. Koretsune, R. Arita, S. Shin, T. Kondo, S. Nakatsuji, Evidence for magnetic Weyl fermions in a correlated metal. *Nat. Mater.* **16**, 1090–1095 (2017).
24. J.-X. Yin, W. Ma, T. A. Cochran, X. Xu, S. S. Zhang, H.-J. Tien, N. Shumiya, G. Cheng, K. Jiang, B. Lian, Z. Song, G. Chang, I. Belopolski, D. Multer, M. Litskevich, Z.-J. Cheng, X. P. Yang, B. Swidler, H. Zhou, H. Lin, T. Neupert, Z. Wang, N. Yao, T.-R. Chang, S. Jia, M. Z. Hasan, Quantum-limit Chern topological magnetism in $TbMn_6Sn_6$. *Nature* **583**, 533–536 (2020).
25. L. B. McCusker, R. B. Von Dreele, D. E. Cox, D. Louër, P. Scardi, Rietveld refinement guidelines. *J. Appl. Cryst.* **32**, 36–50 (1999).
26. J. Rodriguez-Carvajal, Recent advances in magnetic structure determination by neutron powder diffraction. *Physica B* **192**, 55–69 (1993).
27. J. W. Lynn, Y. Chen, S. Chang, Y. Zhao, S. Chi, W. Ratcliff II, B. G. Ueland, R. W. Erwin, Double-focusing thermal triple-axis spectrometer at the NCNR. *J. Res. Natl. Inst. Stand. Technol* **117**, 61–79 (2012).
28. A. Zheludev, *ResLib 3.4 software* (Oak Ridge National Laboratory, Oak Ridge, Tennessee, 2007).
29. G. Kresse, J. Furthmüller, Efficient iterative schemes for ab initio total-energy calculations using a plane-wave basis set. *Phys. Rev. B* **54**, 11169–11186 (1996).
30. J. P. Perdew, K. Burke, M. Ernzerhof, Generalized gradient approximation made simple. *Phys. Rev. Lett.* **77**, 3865–3868 (1996).
31. P. Blaha, K. Schwarz, G. K. H. Madsen, D. Luitz, J. Laskowsk, F. Tran, L. Marks, L. Marks, *An Augmented Plane Wave Plus Local Orbitals Program for Calculating Crystal Properties* (Vienna Univ. of Technology, 2001).

Acknowledgments: We thank P. Nikolic and C. Batista for insightful discussions. **Funding:** N.J.G. and I.I.M. acknowledge start-up funding from George Mason University. I.I.M. additionally acknowledges support from the U.S. Department of Energy through the grant #DE-SC0021089. Work in the Materials Science Division at Argonne National Laboratory (J.F.M. and J.S.J.) was supported by the U.S. Department of Energy, Office of Science, Basic Energy Sciences, Materials Science, and Engineering Division. Work at ORNL (M.A.M.) was supported by the U.S. Department of Energy, Office of Science, Basic Energy Sciences, Materials Sciences, and Engineering Division. The identification of any commercial product or trade name does not imply endorsement or recommendation by the National Institute of Standards and Technology. **Author contributions:** N.J.G. conceived and coordinated the project. N.J.G. and N.T.M. grew the crystals. N.J.G., N.T.M., D.M., and D.C.J. characterized the samples. N.J.G. and M.A.M. performed the magnetic and magnetotransport measurements. J.F.M. contributed to the magnetic and transport measurements. J.S.J. contributed to the transport measurements.

L.P., R.L.D., and J.W.L. carried out neutron diffraction experiments. L.P., M.B., N.J.G., and J.W.L. performed small angle neutron scattering experiment. I.I.M. carried out the first-principles calculations and devised the phenomenological theory. N.J.G. wrote the manuscript with contributions from R.L.D., J.W.L., and I.I.M. All authors contributed to the discussion of the results. **Competing interests:** The authors declare that they have no competing interests. **Data and materials availability:** All data needed to evaluate the conclusions in the paper are present in the paper and/or the Supplementary Materials. Additional data related to this paper may be requested from the authors.

Submitted 11 August 2020
Accepted 2 November 2020
Published 18 December 2020
10.1126/sciadv.abe2680

Citation: N. J. Ghimire, R. L. Dally, L. Poudel, D. C. Jones, D. Michel, N. T. Magar, M. Bleuel, M. A. McGuire, J. S. Jiang, J. F. Mitchell, J. W. Lynn, I. I. Mazin, Competing magnetic phases and fluctuation-driven scalar spin chirality in the kagome metal YMn_6Sn_6. *Sci. Adv.* **6**, eabe2680 (2020).

ScienceAdvances

Competing magnetic phases and fluctuation-driven scalar spin chirality in the kagome metal YMn_6Sn_6

Nirmal J. Ghimire, Rebecca L. Dally, L. Poudel, D. C. Jones, D. Michel, N. Thapa Magar, M. Bleuel, Michael A. McGuire, J. S. Jiang, J. F. Mitchell, Jeffrey W. Lynn and I. I. Mazin

Sci Adv **6** (51), eabe2680.
DOI: 10.1126/sciadv.abe2680

Science Advances
AAAS

advances.sciencemag.org/cgi/content/full/6/51/eabe2680/DC1

Supplementary Materials for

Competing magnetic phases and fluctuation-driven scalar spin chirality in the kagome metal YMn_6Sn_6

Nirmal J. Ghimire*, Rebecca L. Dally, L. Poudel, D. C. Jones, D. Michel, N. Thapa Magar, M. Bleuel, Michael A. McGuire, J. S. Jiang, J. F. Mitchell, Jeffrey W. Lynn, I. I. Mazin

*Corresponding author. Email: nghimire@gmu.edu

Published 18 December 2020, *Sci. Adv.* **6**, eabe2680 (2020)
DOI: 10.1126/sciadv.abe2680

This PDF file includes:

S1. CRYSTAL STRUCTURE REFINEMENT

The crystal structure of the single crystals of YMn_6Sn_6 were verified by Rietveld refinement of a powder x-ray diffraction pattern collected on the ground single crystals at room temperature. Rietveld refinement of a representative powder pattern is depicted in Fig. S1. A previously reported crystal structure (*13*) with space group $P6/mmm$ was used in the refinement. The results of the refinement are presented in Table **S1**. Lattice parameters a = 5.5398(5) Å and c = 9.0203(9) Å are in good agreement with the reported values (*14,17*). A small peak that was not indexed to be of YMn_6Sn_6 (as marked by an asterisk in Fig. S1) was identified to be a Sn peak from the Sn-flux attached on the surface of the crystals. This impurity peak was excluded from the refinement.

S2. NEUTRON DIFFRACTION

One of the central motivations for investigating the properties of YMn_6Sn_6 was to determine the origin of the observed topological Hall effect. One possibility was that a skyrmion lattice formed in the system, and therefore our first neutron experiments were using small angle neutron scattering (SANS) to search for skyrmions with the NG-7 SANS instrument at the NIST Center for Neutron Research using a 9 T horizontal field magnet ($H \parallel [1,1,0]$) and exploring the temperature range from 4 K to 300 K. Figure S2(a) shows a background subtracted image over a wide wave vector range. No large scale magnetic structures were observed such as expected for a skyrmion lattice. Rather, just a single diffraction spot at a rather large (for SANS) wave vector was observed, indicating that long range magnetic order with an incommensurate modulation is realized. Fig. S2(b) shows an example of the field dependence of the magnetic order, demonstrating a complex series of magnetic phase transitions. Figure S2(c) shows cuts through the scattering at a field of 7 T for a series of temperatures, where it was first observed that there are two closely-spaced incommensurate wave vectors. To further elucidate the nature of the magnetic structures as a function of both magnetic field and temperature, wide angle diffraction data were collected as we now describe. Note that uncertainties where indicated represent one standard deviation throughout the manuscript.

Figure S3 shows the variation of the incommensurate Bragg peaks at $(1,\ 1,\ 0 - k_{z,n})$ with

the external magnetic field applied in the ab-plane at 100 K and 256 K, similar to the data presented about (0, 0, $2 - k_{z,n}$) in Figs. 2(b) and (c). The momentum resolution in the measurement about the (1, 1, $0 - k_{z,n}$) peaks is much better than that about the (0, 0, $2 - k_{z,n}$) peaks, and as a result, the separation of $k_{z,1}$ and $k_{z,2}$ at 100 K is clearer in the former case. Determination of peak centering obtained from the fitting of (1, 1, 0 -$k_{z,n}$) is thus unambiguous. We used the distance between the peak centers determined from the fitting of (1, 1, $0 - k_{z,n}$) to distinguish the behavior of the two peaks in (0, 0, $2 - k_{z,n}$) discussed in the main text. Additionally, the full-width-at-half-maxima of the Gaussian fits were fixed to be that of the instrumental resolution as described in the Methods section. The integrated intensity obtained from the Gaussian fits are shown in Figs. S4(b) and (c). It can be seen from these figures that the percent decrease in intensity at the metamagnetic transition H_1 is not as great as the (0, 0, $2-k_{z,n}$) peaks, as expected for a helical to cycloidal transition. Intensities of the peaks measured at (1, 1, $0 - k_{z,n}$) are much weaker compared to the peaks measured at (0, 0, $2 - k_{z,n}$), but it is still clear that at 6 T, $k_{z,2}$ has practically no intensity and the intensity of $k_{z,1}$ is very weak. As the commensurate peaks emerge at 6 T [Figs. 3(b) and S4(a)], it suggests that they appear at the cost of the incommensurate peaks.

In Fig. S5, we plot the experimental ratio of intensity above versus below H_1 together with the corresponding calculated ratios. This plot supports the first principles calculations results discussed in the main text of helical to cycloidal spin flop at H_1. Given a k_z and any α value (the rotation angle between Mn layers separated by pure Sn layers), the calculated cycloidal:helical intensity ratio is 0.5 for (0, 0, L)-type peaks. This is because in the helical state, all spins lie perpendicular to (0, 0, L)-type scattering vectors, and neutrons are only sensitive to the component of a spin which is perpendicular to the scattering vector. When the moments flop into the $(1, 1, 1)$ plane and the structure becomes cycloidal, half of the total spin magnitude is now projected along (0, 0, L), thus reducing the intensity by half. There is generally much less of an intensity suppression after the transition for Bragg peaks at (H, H, L) positions where H is not equal to 0. This is because for a specific k_z, the cycloidal:helical structure factor ratios for a given peak do not change regardless of the value of α. There are, however, slight differences in the ratios for different wave vectors, although they are small for the range of k_z observed in YMn_6Sn_6. The calculations used the different $k_{z,n}$ values from the neutron data for the different temperatures and on either side of H_1.

The (0, 0, L)-type peaks decrease in intensity more relative to the (H, H, L) ($H \neq 0$) peaks across the H_1 boundary, consistent with what would be observed for a helical to cycloidal spin-flop transition. Combined with the theoretical results, the neutron data do support the proposed helical to cycloidal spin-flop transition at H_1, especially when considering other complex incommensurate magnetic structures, such as the fan or spin density wave, which would bear the hallmark of Bragg peak harmonics and any harmonics are absent in the data presented here.

Additionally, we expect that immediately following the spin-flop transition, the cycloidal arrangement of spins would begin to cant along **H**, forming a transverse conical structure. We confirmed this canting by tracking the net induced ferromagnetic component at the (0, 0, 4) Bragg peak as a function of applied magnetic field. In zero field, the intensity is purely nuclear in origin, with a field-induced intensity simply adding to the structural part. We see an abrupt emergence of an induced net ferromagnetic component at H_1 for the 100 K and 256 K data, as shown in Figs. S6(a), and (b), respectively. We note that the 256 K data in Fig. S6(b) were taken with coarser instrumental resolution as can be discerned by the x-axes in Figs. S6(a) and (b). The integrated intensity with respect to the zero-field intensity is shown for both temperatures in Fig. S6(c). The abrupt increase in intensity is indicative of a sudden canting of the moments towards the applied field direction, $[1, \bar{1}, 0]$, and the magnitude of this projection, in $\mu_B^2 \mathrm{Mn}^{-1}$, is displayed on the right axis of Fig. S6(c). Note that the induced moment along the applied field direction is smaller at the higher temperature as expected, and both behaviors are completely consistent with bulk magnetization measurements presented in the main text [Fig. 2(a)].

S3. FIRST PRINCIPLES CALCULATIONS

Total energies of 10 different collinear (α and β defined below are either 0 or 180°) magnetic patterns were calculated in a supercell containing 8 Mn layers. Individual layers were ordered ferromagnetically, and the selected patterns were: *uddddddu*, *udddddud*, *uddddudd*, *uddduuud*, *uddduuud*, *ududdudu*, *udududdu*, *udududud*, *uudduudd*, *uuduuudd*, *uuuuuuuu*, where u stands for an up-polarized layer, and d for down-polarized. These were fitted to the

following Hamiltonian:

$$2E = J_1 \cos\alpha + J_2 \cos\beta + 2J_3 \cos(\alpha+\beta) + J_4 \cos(2\alpha+\beta) + J_5 \cos(\alpha+2\beta) + 2J_6 \cos(2\alpha+2\beta) \quad \text{(S1)}$$

where J_i are exchange interactions defined in Fig. S7, E is the energy per layer, and the angles α and β define rotations between the planes bridged by Sn_3 or Sn_2Y layers [see Fig. 1(a)]. At low temperature the wave vector is $\approx \pi/2c$. Fitting quality is very high, as shown in Fig. S8 (blue circles). The resulting values for J_{1-6} are $-50.9,\ 9.1,\ 4.1,\ -4.0,\ -7.5$, and -3.4 meV. An immediate observation is that, indeed, J_1 is strongly ferromagnetic, J_2 and J_3 are both antiferromagnetic, but (i) their absolute values are quite far from the stability range of any spiral and (ii) longer-range interactions, especially J_5, are very important. A closer look reveals that the main factor preventing the formation of a spiral is the large J_1. Indeed, for a ferromagnetic J_1, a spiral can only be stable if $J_2/2(|J_1|+J_2) < J_3/J_1 < J_2/2(|J_1|-J_2)$. This range, for $J_2 \ll J_1$, becomes infinitely narrow, $J_2 - J_2^2/J_1 < 2J_3 < J_2 + J_2^2/J_1$. Including the long-range interactions does not change this picture: the ground state is the collinear *uudd* pattern.

In many systems, the addition of Coulomb correlations reduces short-range magnetic couplings, but less so the long range ones. With this in mind, we repeated the calculations by adding a Hubbard U in the common LDA+U approximation. Figure S8 (symbols other than blue circles) shows the fit quality, which is still high. Figure S9 shows how the fitted parameters vary as a function of the effective $\tilde{U} = U - J$.

It is instructive to look at the phase diagram in the "reduced" (J_1, J_2, J_3 only) model. Figure S10 shows where our calculated effective exchange parameters fall at different $\tilde{U} \approx 0.4$ eV and for ≈ 0.6 eV indeed a spiral is stable, and another for very large (likely unphysical for a good metal) U. It is also useful to compare the calculated magnetic moments on Mn with the experimental number of $M_{\rm exp} = 2.1$. The fact that even at $\tilde{U} = 0$ the moment is overestimated indicates a strongly fluctuating system and weak correlations.

On the other hand, an effective magnetic moment of $\mu_{eff} = 3.6\ \mu_B$ was extracted from the high-temperature susceptibility (*33*), consistent with a spin $S = 3/2$ (magnetic moment $3\ \mu_B$). Thus one can conclude that, despite the fact that for $\tilde{U} \sim 2-3$ eV the system re-enters a spiral region, this part of the calculated phase diagram is unphysical. However, the range of 0.4 – 0.6 eV yields $M \sim 2.7\ \mu_B$ (Fig. S11) consistent with μ_{eff}, and, after being

reduced by fluctuations, with $M_{\rm exp}$. As Fig. S12 illustrates, the calculated spiral angles at $\tilde{U} = 0.4$ eV are $\alpha = -22^\circ$ and $\beta = 138^\circ$. Aside from some overestimate in β, the overall agreement is good.

Plotting J_i as a function of distance clearly shows that it is inconsistent with the Ruderman–Kittel–Kasuya–Yosida (RKKY) expression; in particular, it decays much more slowly than $1/d^4$. Nevertheless, there is no question that the interaction is transferred by conduction electrons. The conclusion is then that the Fermi surface must be rather complicated, and indeed it is. Another complication is that the standard RKKY formalism describes the interaction of localized moments in a nonmagnetic matrix. This is, obviously, inapplicable here. The closest analogy would be to start with a ferromagnetic state and see whether it may be unstable against the formation of a spin density wave (SDW). To address this, we computed the Fermi surface, which is shown in Figs. S13(a) and (b).

Examining the Fermi surfaces, we see immediately that the spin-down surface is somewhat 2D and does not bear any obvious signature of nesting. The spin-up surface, on the other hand, is rather 3D, and has two pockets, one electron and one hole, which nest rather well with $q_z(\mathring{A}^{-1}) = 0.235\frac{2\pi}{c}$, which agrees reasonably with the spiral vector in the experiment. This is illustrated in Fig. S13(c), showing a 2D cut of the pockets in question. Of course, this instability, which is similar in spirit, but rather different in details from RKKY, is superimposed on top of other, short range interactions, which affect the final outcome.

S4. MEAN FIELD THEORY IN EXTERNAL MAGNETIC FIELD

Previous analyses were based on the assumption that only two ground states compete, a longitudinal conical spiral (LCS), where the field is oriented along the spiral vector, and the distorted spiral (DS) (*18*) where the field is applied normal to the spiral pitch. In the former, each moment is rotated out of the plane by the same amount to form a component parallel to the field. In the latter, the moments rotate in the plane, but retain the general spiral structure. We will show that this does not exhaust possible magnetic states.

Analyzing the complete model of Eq. S1 with an external field in an arbitrary direction is too cumbersome; for simplicity, we will reduce the model to the "standard" $J_1 - J_2 - J_3$ one, keeping in mind that the physics of the spin-flop and spin-flip transitions is roughly the same. We then adjust the parameters to generate a SDW with $q \approx (0, 0, 0.25)$, and the pitching

angles $\alpha = -20^\circ$ and $\beta = 110^\circ$ ($\alpha + \beta = 90^\circ$), that is, $J_2/J_1 = -0.364$, $J_3/J_1 = 0.171$ (and, $J_1 < 0$). For reference, the angles are in agreement with published analyses (*18*),

$$\alpha = -\mathrm{sign}(J_1 J_3) \cos^{-1}\left(\frac{J_2 J_3}{J_1^2} - \frac{J_3}{J_2} - \frac{J_2}{4J_3}\right), \tag{S2}$$

$$\beta = \cos^{-1}\left(\frac{J_3 J_1}{J_2^2} - \frac{J_1}{4J_3} - \frac{J_3}{J_1}\right), \tag{S3}$$

$$\alpha + \beta = \cos^{-1}\left(\frac{J_1 J_2}{8J_3^2} - \frac{J_2}{2J_1} - \frac{J_1}{2J_1}\right). \tag{S4}$$

First, let us calculate the energy of the LCS state. Taking the same rotation angle θ for all moments and assuming the ideal in-plane ferromagnetic order, we can write the total energy per one 1×1×4 supercell as

$$E_{LCS} = 4(J_1 \cos\tau - J_2 \sin\tau) M_{||}^2 + 4(J_1 + J_2 + 2J_3) M_\perp^2 - 8HM_\perp \tag{S5}$$

where $\tau = -\alpha = \beta - 90^\circ = 20^\circ$, $M_{||} = \cos\theta$, and $M_\perp = \sin\theta$ (as before, we normalize all interactions to unit moment). In the following we shall simplify notations by using $e = E/|J_1|$, $j_{2,3} = J_{2,3}/J_1$, and $h = H/|J_1|$. The sign is kept in the second definition to harmonize notations with Refs. *18* and *34*. Minimizing with respect to θ, and using the selected parameters, we find

$$e_{LCS} = -4.257 - 46.443h^2. \tag{S6}$$

The angle θ changes gradually from $\pi/2$ to 0, and saturates at h =0.086. Next, we consider the field applied in the plane. Since the leading wave vector at low temperature, experimentally is close to (0, 0, 0.25), and changes little with magnetic field (notwithstanding important, but small changes), we will consider a *commensurate* SDW in the $1 \times 1 \times 4$ supercell, and, contrary to the previous works, we shall assign different angles ϕ_i to each of the eight sites. In the absence of a field, $\{\phi_2, \phi_3, \phi_4, \phi_5, \phi_6, \phi_7, \phi_8\} - \phi_1 = \{-\tau, \pi/2, \pi/2 - \tau, \pi, \pi - \tau, 3\pi/2, 3\pi/2 - \tau\}$. The total energy now looks like ($\phi_9 = \phi_1$)

$$\begin{aligned} e_{DS} = &- \sum_{j=1,4} \cos(\phi_{2j} - \phi_{2j-1}) - j_2 \sum_{j=1,4} \cos(\phi_{2j} - \phi_{2j+1}) \\ &- j_3 \sum_{i=1,8} \cos(\phi_i - \phi_{j+2}) - h \sum_{i=1,8} \cos(\phi_i). \end{aligned} \tag{S7}$$

Minimizing this expression with respect to ϕ_i reveals two interesting transition [Figs. 4(a) and (c)]. At $h = h_f \approx 0.035$ the energy slope changes discontinuously, *i.e.*, the magnetization

experiences a jump. At $h = h_3 = 0.086$ (which represents H_3 in the phase diagram), the moment saturates, and therefore $\chi = dM/dH$ has a discontinuity. A closer inspection reveals that up to h_f the grounds state is indeed a slightly distorted spiral. Between h_f and h_3, however, it is a qualitatively different state, which we call fan-like (FL) phase, where the moments 1 and 2 are aligned ferromagnetically, and so are 5 and 6. They are gradually rotating with the field until they become parallel to the latter at h_3. At the same time, the pairs 3 and 4, and 7 and 8 are canted from the field in opposite directions. Thus, the moments form the following angles with the field: $(\gamma, \gamma, -\delta, \delta, -\gamma, -\gamma, \delta, -\delta)$. Immediately after the transition their values are $\gamma = 77.25^\circ$ and $\delta = -10.06^\circ$. The normalized energy $e = E/J_1$ as a function of the normalized field $h = H/J_1$ of the LCS and planar (the planar state is distorted spiral below, and a fan-like structure above the kink at h_f) phases are shown by the solid red line and dotted blue line, respectively in Fig. 4(a) of the main text.

However, without taking into account any anisotropy, E_{LCS} is alway lower than either E_{DS} or E_{FL}, so the former would immediately flop and stay as such at all fields. So, let us include an easy-plane anisotropy, by adding a penalty term $KM_\perp^2$. The distorted spiral state is not affected. The spin-flopped longitudinal conical spiral, competing with the distorted spiral, is the transverse conical spiral, as described in the main text. Its energy is

$$\begin{aligned} E_{TCS} = {} & 4(J_1 \cos\tau - J_2 \sin\tau) M_{||}^2 + 4(J_1 + J_2 + 2J_3) M_\perp^2 \\ & - 8HM_\perp + 8KM_\perp^2. \end{aligned} \tag{S8}$$

Since the average value of $M_\perp^2$ in the transverse conical spiral state is $M^2/2$, the penalty term for $h = 0$ is $8KM^2/2 = 4K^2$ (normalizing to $M = 1$). This penalty will gradually decrease with h, as the canting toward the field direction increases. In short, it amounts to just adding a penalty term equal to $const \times [1 - (h/h_{sat})^2]$ to Eq. S5. Energy of the transverse conical spiral phase as a function of the magnetic field will then be different, which is shown in Fig. 4(a) as the green solid line.

At large fields, close to saturation, the energy gain derived from a larger spin susceptibility in the transverse conical spiral phase is nearly lost, and at some critical field $h_2 \approx 0.072$ (H_2 in the phase diagram) it becomes energetically favorable to regain the anisotropy energy by flopping again into the *ab*-plane, into the fan-like phase (of course, the angles γ and δ are now very small).

So the magnetic phases obtained are:

1) For the magnetic field along the c-axis: only the longitudinal conical spiral phase is possible, and it gradually changes until the saturation is reached at $h = h_3$. 2) For the magnetic field in the ab-plane: At very small fields the state is distorted spiral. In this phase, magnetization increases with a rather small slope until the spin-flop field, proportional to $\sqrt{K}$, is reached ($K = 0.01J_1$ was used in the plot, inspired by the calculated value of $K \sim 0.2$ meV, and then $h_{flop} = h_1 \approx 0.018$), at which point the state discontinuously transforms into the transverse conical spiral phase *via* a spin flop. Highly unusual, it flops again at the field h_2 into the fan-like phase (again, for our selection of K, it is ≈ 0.072), and finally saturates at $h_3 = 0.086$.

Let us now estimate the effect of the two spin-flops at, h_1, and h_2, on the spiral vector. In the above calculations we absorbed all magnetic anisotropies into one single-site term. However, there are no *a priori* arguments that anisotropic exchange (of the form $J^z M_i^z M_j^z$) should be small compared to the single-site anisotropy. On the contrary, cases are known, when light magnetic $3d$ ions are bridged by heavy nonmagnetic elements (as Sn and Y in our case) and the anisotropic exchange dominates, for instance in CrI_3, which, as well as YMn_6Sn_6, has a large magnetic moment.

Dividing the magnetic anisotropy into the single-site and exchange parts would not change the calculated phase diagram, except for one aspect. Indeed, while the onsite anisotropy does not change, in the lowest order, the spiral pitch, the anisotropic exchange does. Essentially, it adds an $antiferromagnetic$ component to the ferromagnetic bonds and a $ferromagnetic$ component to the antiferromagnetic bonds. Assuming that the leading contribution comes from the largest J (which is ferromagnetic J_1), one can calculate the derivative $d\cos(\alpha + \beta)/dJ_1 = J_2/8J_3^2 + J_2/2J_1^2 - 1/2J_2 = J_1^{-1}(j_2/8j_3^2 + j_2/2j_1^2 - 1/2j_2 = -0.364J_1^{-1}$. Adding an antiferromagnetic contribution to J_1 (i.e., $\Delta J_1 > 0$) will have a negative effect $\cos(\alpha + \beta)$, that is to say, $\alpha + \beta$ will be larger, and so will be the spiral q, in agreement with the experiment.

Calculations give $K \approx -0.12$ meV/Mn (easy axis) and $(J_1^z + J_2^z)/2 \approx 0.34$ meV (easy plane). This contribution is positive, i.e., antiferromagnetic. Assigning it entirely to J_1, we get J_1^z of the right sign, and $J_1^z/J_1 \sim 0.34/51 \sim 0.7\%$, in qualitative agreement with the experiment.

S5. THEORY OF SPIN CHIRALITY IN YMn_6Sn_6

We now present a phenomenological theory of fluctuation-generated chirality and the topological Hall effect (THE) on a background of a static cycloidal or transverse conical magnetic spiral, which is observed at finite temperatures in an external magnetic field. We will assume that the amplitude of the Mn moments is constant (*i.e.*$|\mathbf{M}| = 1$). The four phases of interest in YMn_6Sn_6 are [see Figs. 2 and 4(a)]:

1. A longitudinal conical spiral (LCS) propagating along z in the field parallel to z, where the magnetic moment is described, in a continuous approximation, as

$$\mathbf{M} = \mathbf{M}_z + \mathbf{m} \tag{S9}$$

$$\mathbf{M}_z = const \tag{S10}$$

$$\frac{\partial \mathbf{m}}{\partial z} = m \times \mathbf{z}, \tag{S11}$$

where $\mathbf{M}_z \parallel \mathbf{z}$, and $\mathbf{m} \perp \mathbf{z}$. Here and below $\mathbf{z}$ is the unit vector.

2. A distorted spiral (DS) that appears in the in-plane field (parallel to x,) and below the first spin-flop (*i.e.*H_1) transition. In the first approximation,

$$\mathbf{M} = \tilde{\mathbf{M}} + \mathbf{m} \tag{S12}$$

$$\frac{\partial \tilde{\mathbf{M}}}{\partial z} = \tilde{\mathbf{M}} \times \mathbf{z} \tag{S13}$$

$$\mathbf{m} = \tilde{M}_y \tilde{\mathbf{M}} \times \mathbf{z}, \tag{S14}$$

where $\tilde{\mathbf{M}} \perp \mathbf{z}$ and $\mathbf{m} \perp \mathbf{z}$.

3. A fan-like (FL) phase. The FL phase is fully coplanar and the magnetic moments do not change along c, so it cannot support any scalar chirality.

4. A transverse conical spiral (TCS) that appears in the in-plane field (parallel to x :)

$$\mathbf{M} = \mathbf{M}_x + \mathbf{m} \tag{S15}$$

$$\mathbf{M}_x = const \tag{S16}$$

$$\frac{\partial \mathbf{M}}{\partial z} = \frac{\partial \mathbf{m}}{\partial z} = \mathbf{m} \times \mathbf{x}, \tag{S17}$$

where $\mathbf{M}_x \parallel \mathbf{x}$, and $\mathbf{m} \perp \mathbf{x}$.

We will now use the standard expression for the topological field, see *e.g.*, Eq. B4b in Ref. *2* (omitting the coefficient of 2):

$$b_\alpha = \varepsilon^{\alpha\beta\gamma}\, \mathbf{M} \cdot (\partial_\beta \mathbf{M} \times \partial_\gamma \mathbf{M}). \tag{S18}$$

In the first case described above, that is, for an external field in the z-direction, the field couples with b_z, and

$$b_z \;=\; \mathbf{M}\cdot(\partial_x\mathbf{M}\;\times\;\partial_y\mathbf{M}). \tag{S19}$$

In the ground state both $\partial_x\mathbf{M}$ and $\partial_y\mathbf{M}=0$, so generating a nonzero b_z requires exciting simultaneously two types of magnons, with two different in-plane vectors, which is an unlikely case.

In cases 2-4, *i.e.*, for an external field along x-direction, only b_x couples with the external field, so without losing generality we can rewrite it as:

$$b_x \;=\; \mathbf{M}\cdot(\partial_y\mathbf{M}\times\;\partial_z\mathbf{M}) = \partial_y\mathbf{M}\cdot(\partial_z\mathbf{M}\times\mathbf{M}). \tag{S20}$$

In the ground state $\mathbf{M}$ only varies with z, so this expression is obviously zero. In a planar-helical ($\mathbf{H}=\mathbf{0}$) state $\partial_z\mathbf{M}\times\mathbf{M}$ is parallel to z, and averages to zero over all planes. So, let us concentrate on the state (4). Let us then write $\mathbf{M}$ as

$$\mathbf{M} = M_x\mathbf{x}+\mathbf{m}+\boldsymbol{\mu} \tag{S21}$$

where, as mentioned, $\mathbf{m}\perp\mathbf{x}$, and $\boldsymbol{\mu}$ represents a magnon propagating along y (in order to have nonzero $\partial_y\mathbf{M}$) in a plane defined by a vector $\boldsymbol{\omega}$**,** such that $\boldsymbol{\omega}\propto k_y$. Then

$$\frac{\partial\mathbf{M}}{\partial z} = \frac{\partial\mathbf{m}}{\partial z} \;= \mathbf{m}\times\mathbf{x} \tag{S22}$$

$$\frac{\partial\mathbf{M}}{\partial y} = \frac{\partial\boldsymbol{\mu}}{\partial y} \;= \boldsymbol{\mu}\times\boldsymbol{\omega} \tag{S23}$$

Let us now calculate b_x

$$b_x = (M_x\mathbf{x}+\mathbf{m}+\boldsymbol{\mu})\cdot((\boldsymbol{\mu}\times\boldsymbol{\omega})\;\times\;(\mathbf{m}\times\mathbf{x})) \tag{S24}$$

$$= \boldsymbol{\mu}\cdot([(\boldsymbol{\mu}\boldsymbol{\omega})\cdot\mathbf{x}]\mathbf{m}-[(\boldsymbol{\mu}\times\boldsymbol{\omega})\cdot\mathbf{m}]\mathbf{x}) \tag{S25}$$

where the terms linear in $\boldsymbol{\mu}$ are dropped because they average to zero upon integrating over y. Continuing with the expansion,

$$b_x = (\boldsymbol{\mu}\cdot\mathbf{m})[\boldsymbol{\mu}\cdot(\boldsymbol{\omega}\times\mathbf{x})]-(\boldsymbol{\mu}\cdot\mathbf{x})[\boldsymbol{\mu}\cdot(\boldsymbol{\omega}\times\mathbf{m})] \tag{S26}$$

It is important to note that we can consider each ab plane independently, as they are capable of fluctuating independently. Let us for simplicity consider the case $\boldsymbol{\omega}\;||\;z$. Then

$$b_x = (\boldsymbol{\mu}\cdot\mathbf{m})[\boldsymbol{\mu}\cdot y]-(\boldsymbol{\mu}\cdot\mathbf{x})[\boldsymbol{\mu}\cdot(\boldsymbol{\omega}\times\mathbf{m})] = k_y m_z\mu^2 \tag{S27}$$

Now for $\boldsymbol{\omega} \parallel y$, after averaging over y, we get

$$b_x = -k_y m_z \mu^2 \tag{S28}$$

and, if $\boldsymbol{\omega} \parallel x$, $b_x = 0$. We saw that there are some magnons in the system that propagate along y and can generate a topological magnetic field b_x, which couples to the external field H_x. By definition, the energy cost to excite such a magnon is $Ak_y^2 JM^2$, where J is the ferromagnetic exchange coupling in the plane. As we have seen, $b_x = Bk_y$ for magnons with some polarization planes and $-Bk_y m_z$ for others. The coupling term must be $CH_x k_y$. The constants B and C are proportional to m_z, and are different for each plane. Let us calculate the expectation value for the $\langle b_x \rangle$ for one plane and one type of magnons:

$$\langle b_x \rangle = \frac{\int Bk_y e^{-Ak_y^2 J/T}(e^{CH_x k_y/T} - e^{-CH_x k_y/T})dk_y}{\int e^{-Ak_y^2 J/T}(e^{CH_x k_y/T} + e^{-CH_x k_y/T})dk_y} \tag{S29}$$

$$= \frac{\int Bk_y e^{-Ak_y^2 J/T} \sinh(CH_x k_y/T)dk_y}{\int e^{-Ak_y^2 J/T} \cosh(CH_x k_y/T)dk_y} \tag{S30}$$

$$\approx \frac{\int Bk_y e^{-Ak_y^2 J/T}(CH_x k_y/T)dk_y}{\int e^{-Ak_y^2 J/T}dk_y}. \tag{S31}$$

In the last line we made use of the fact that $J \gg T$. From that,

$$\langle b_x \rangle = BCH_x T/AJ = const \cdot TM_z^2 H_x = const \cdot (1 - M^2/M_s^2)TH_x, \tag{S32}$$

where M_s is the saturated magnetization.

In a nutshell, the procedure includes the following steps:

1) Since every ordered magnet, and, in particular, an ordered ferromagnetic plane, includes thermally excitable spin waves (in the literature also called spin excitations, spin fluctuations, or simply magnons), we want to include the potential interaction of these with an external magnetic field. Note that, having no net magnetization, each individual magnon has no Zeeman interaction with the external field.

2) Each individual magnon, at a given temperature, is characterized, by definition, by its amplitude $\boldsymbol{\mu}$ and propagation wave vector $\mathbf{k}$ (also by its frequency, but this does not affect our consideration).

3) We show that each magnon, given the specific underlying magnetic structure observed in the TCS (and only in the TCS) phase interacts with the external field. We further show that this interaction is proportional to the y-component of the $\mathbf{k}$ -vector, k_y, so that two

magnons with opposite k_y-projections, k_y and $-k_y$, have an opposite (in sign) interaction with the external field.

4) With this, and only this information, we can calculate the thermodynamic average of the corresponding chiral field (chiral order parameter) by evaluating the magnon partition function. In doing so, we integrate over the entire (albeit unknown) spin wave spectrum of the system, that is, over all possible k_y. The evaluation can be performed analytically and yields Eq. S32.

A requirement for this scenario is a conical spiral rotating in a plane perpendicular to the external field. It is also essential that the coupling between the planes is weak, allowing magnons to be excited independently in each plane. It is also obvious from the general theory of the topological Hall effect that conduction electrons should be strongly coupled to the magnetic moments. This implies that, as in MnSi (*2*), they belong to the same system and have strong Hund's rule coupling. This is fulfilled here because both the moments and the conductivity are due to Mn d-electrons, but may not work well for, say, rare earth based spiral magnets. In any event, the scale of the effect must be very material-dependent (coefficients B and C above), and its microscopic evaluation may be challenging.

S6. TOPOLOGICAL HALL EFFECT

The Hall effect, in general, is an intrinsic property of a conductor due to the Lorentz force experienced by the charge carriers. In systems with spontaneously broken time-reversal symmetry, an additional contribution, independent of the Lorentz force, is observed which is proportional to the magnetization M and is called the anomalous Hall effect (AHE) (*35*). In materials with spin textures allowing a non-zero scalar spin chirality defined by $\boldsymbol{S}_i \cdot (\boldsymbol{S}_j \times \boldsymbol{S}_k)$, where i, j, k are neighboring spins (equivalent, in the continuous approximation, to Eq. S18), an additional component of the Hall effect is permitted due to the real-space Berry phase called the topological Hall effect (*3,36*). Thus, a Hall resistivity can be expressed as:

$$\rho_H = \rho^O + \rho^A + \rho^T. \tag{S33}$$

Here $\rho^O = R_0 B$ is the ordinary Hall resistivity, where R_0 is the coefficient defined by the number of carriers (weighted with their mobility, for a multiband metal), $B = \mu_0 H$, and H

is the external magnetic field. $\rho^A = R_s \mu_0 M$ is the conventional anomalous Hall resistivity where R_s is the coefficient of the conventional AHE. ρ^T is the Hall resistivity contribution from the THE. R_S and R_0 can be estimated from the high magnetic field component of the magnetization and the Hall resistivity (in the forced ferromagnetic state where the magnetization saturates), where $\rho^T = 0$. Thus, Eqn. S33 takes the form:

$$\rho_H = R_0 B + \mu_0 R_s M. \tag{S34}$$

The intercept of ρ_H/M vs B/M gives $\mu_0 R_s$ while the slope gives R_0. The R_0 estimated this way is correct in the forced ferromagnetic (FF) state. However, we cannot assume the same in the low field region where the Fermi surface (and hence the carrier concentration) is different from that in the FF state. To address this discrepancy, we use the following principle to estimate the normal component of the Hall resistivity that needs to be subtracted (together with the anomalous Hall resistivity) from the measured Hall resistivity to get the topological contribution. Despite M (and thus ρ^A) changing at H_1 nearly discontinuously, up to a small spin-orbit coupling there is no discontinuity in the number of carriers. At H_2, in principle, there might be a discontinuous change in R_0, but since both TCS and FL phases at this point only slightly deviate from the FF state, this change must be small. Thus, to a good accuracy, we can assume that R_0 changes smoothly between the low-field regime ($H < H_1$), where we can estimate it from the difference between ρ_H and ρ^A, and the high-field regime, where it is the only component changing. We estimated the smooth change of the normal component of the Hall resistivity by interpolating a cubic spline between H_1 and H_2 in the $\rho_H - \rho^A$ data. The measured ρ_H and its different components are shown in Fig. S14(a). Together with ρ^O estimated as explained above (green solid line labelled 1), we also show, for comparison, ρ^O obtained by using a simple linear interpolation between H_1 and H_2 in the $\rho_H - \rho^A$ data (orange dashed line labelled 2), and ρ^O calculated using $\rho^O = R_0 B$, where R_0 is obtained in the FF state (brown dashed line labelled 3). The THE obtained using #1 and #3 ρ^O are depicted in Figs. S14(c) and (d), respectively. The amplitude of the THE obtained by using #3 ρ^O is slightly larger than that using #1 ρ^O, which is essentially due to an improper subtraction of the normal Hall component in the former case as can be seen in Fig. S14(d), where using #3 ρ^O still gives some THE contribution below H_1, where it is not expected. The amplitude of the THE obtained using #2 ρ^O lies between that obtained with the other two ρ^O (not shown).

In Fig. S14(b), we show the calculated THE using Eqn. S32 from the theoretical model. As the THE is proportional to $\langle b_x \rangle$, in the calculation we used:

$$\rho^T = \kappa(1 - M^2/M_s^2)TH \tag{S35}$$

where M is the magnetization measured in the magnetic field H, M_s is the saturated magnetization, T is temperature, and k is the proportionality constant. In the calculation, the experimental magnetization data measured at $T = 245$ K are used (black solid line). It is to be noted that Eqn. S35 is valid only in the TCS phase i.e. between H_1 and H_2. Therefore, after calculating ρ^T in the entire field range, we determined the ρ^T obtained outside the TCS phase as a background by interpolating a straight line between H_1 and H_2 (dashed pink line) and subtracted the background to obtain the THE in the TCS phase (solid blue line). This theoretical ρ^T is compared to the experimental data in Fig. S14(c), which is also shown in Fig. 4(d). In Fig. S14(d), we compare the theoretical THE with the experimental THE obtained by using #3 ρ^O discussed above. From Figs. S14(c) and (d), we see that the theoretical model describes the experimental data fairly well irrespective of the method used to estimate the normal Hall component (which is much smaller than the THE). The only difference in the calculated THE in these two cases is the proportionality constant κ. Inset of Fig. 4(d) shows the temperature dependence of ρ^T between 100 K and 250 K at the magnetic field of 4 T, which is also in good agreement with the theoretical model given by Eq. S35 (or Eq. S32). Temperature dependence of the coefficients of normal Hall resistivity (R_0) and the anomalous Hall resistivity (R_s) obtained during the estimation of ρ^T are depicted in Fig. S15. Both ρ^T and R_0 are consistent with the previously reported values (*16*).

To provide further evidence of the THE in YMn_6Sn_6 for the in-plane magnetic field, we show the Hall resistivity measured with the magnetic field in the *ab*-plane and along the *c*-axis in Fig. S16(a). This shows that a topological Hall contribution appears between around 2 T and 5 T only in the case when the magnetic field is applied in the *ab*-plane. The corresponding magnetization data for comparison are presented in Fig. 2(a). The Hall resistivity measured with magnetic field applied in the *ab*-plane at 5 K and 245 K is presented in Fig. S16(b) and the corresponding magnetization data are presented in Fig. S16(c). The difference in magnetization between 5 K and 245 K below 6 T is small, but the Hall resistivity at 245 K is highly enhanced as compared to that at 5 K, which also supports

the presence of a topological contribution to the Hall resistivity at 245 K.

TABLE S1 : Rietveld refinement data. Selected data from rietveld refinement of powder x-ray diffraction collected on ground crystals of YMn_6Sn_6. Atomic coordinates are 0, 0, 0 for Y; $\frac{1}{2}$, 0, z for Mn; 0, 0, z for Sn(1); $\frac{1}{3}$, $\frac{2}{3}$, $\frac{1}{2}$ for Sn(2); and $\frac{1}{3}$, $\frac{2}{3}$, 0 for Sn(3).

Space group	*P6/mmm* (No. 191)
Unit cell parameters	$a = 5.5398(5)$ Å
	$c = 9.0203(9)$ Å
R_{WP}	16.1 %
R_B	7.45 %
R_F	6.26 %
χ^2	1.07
Mn z coordinate	0.24587(20)
Sn(1) z coordinate	0.33679(15)

TABLE S2 : Exchange and single-ion energies. Calculated exchange and single-ion energies for the "Full", "reduced", and "minimal" models.

	Full model	Reduced Model	Minimal model
J_1	-12.86	-12.86	-12.86
J_2	7.26	4.66	4.66
J_3	-0.06	-2.20	-2.20
J_4	0.06	-	-
J_5	-0.16	-	-
J_6	0.54	-	-
J_p	-53	-53	-53
K	-0.31	-0.31	0.19
J^z	0.50	0.50	-

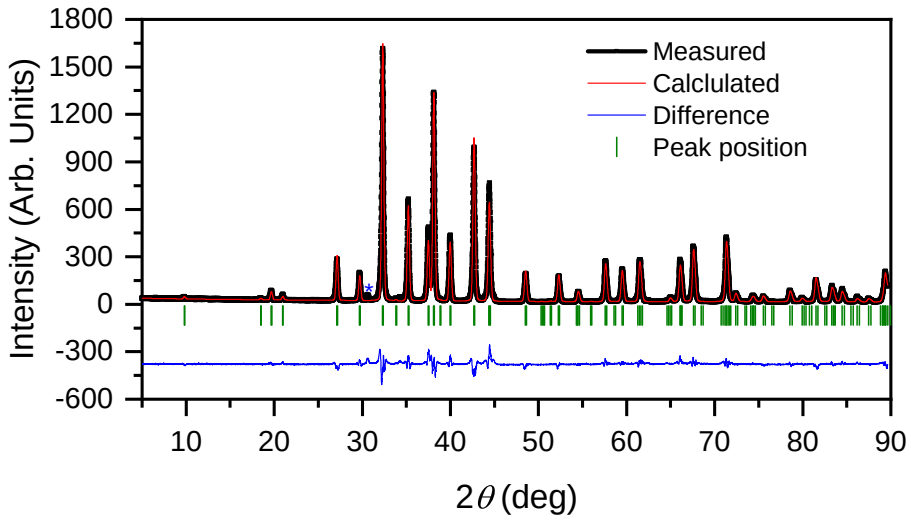

FIG. S1 : X-ray powder diffraction pattern of YMn_6Sn_6. Rietveld refinement of the x-ray powder pattern of YMn_6Sn_6 measured at room temperature. The asterisk ($*$) indicate an impurity peak from the Sn-flux.

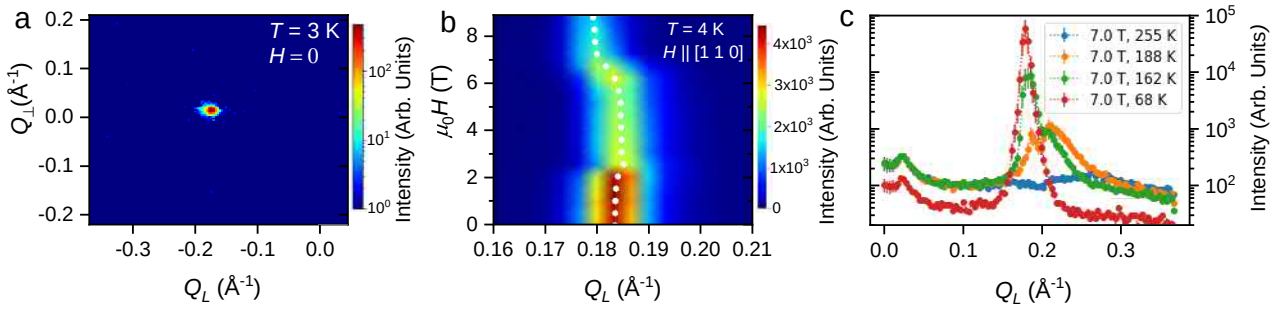

FIG. S2 : Small angle neutron scattering (SANS) of YMn_6Sn_6 . (a) Background-subtracted SANS image on the two-dimensional position sensitive detector at 4 K and without a magnetic field applied. The data show a single incommensurate magnetic peak at a wave vector of $Q = 0.184$ Å^{-1}, corresponding to a real-space modulation of 34 Å. No evidence for a skyrmion lattice was found at any temperature or field. (b) Intensity-Q map of the field dependence of the Bragg peak at 4 K, revealing a series of phase transitions. The white dots are a guide to the peak center. (c) Cuts of the observed intensity through the magnetic peak at 7 T and for a series of temperatures, where it was discovered that at higher temperatures there are two closely-spaced incommensurate peaks. Subsequent wide-angle high resolution diffraction data revealed that there are two wave vectors at all temperatures. Note that the apparent peak at very small Q is simply due to an incomplete subtraction around the beam stop.

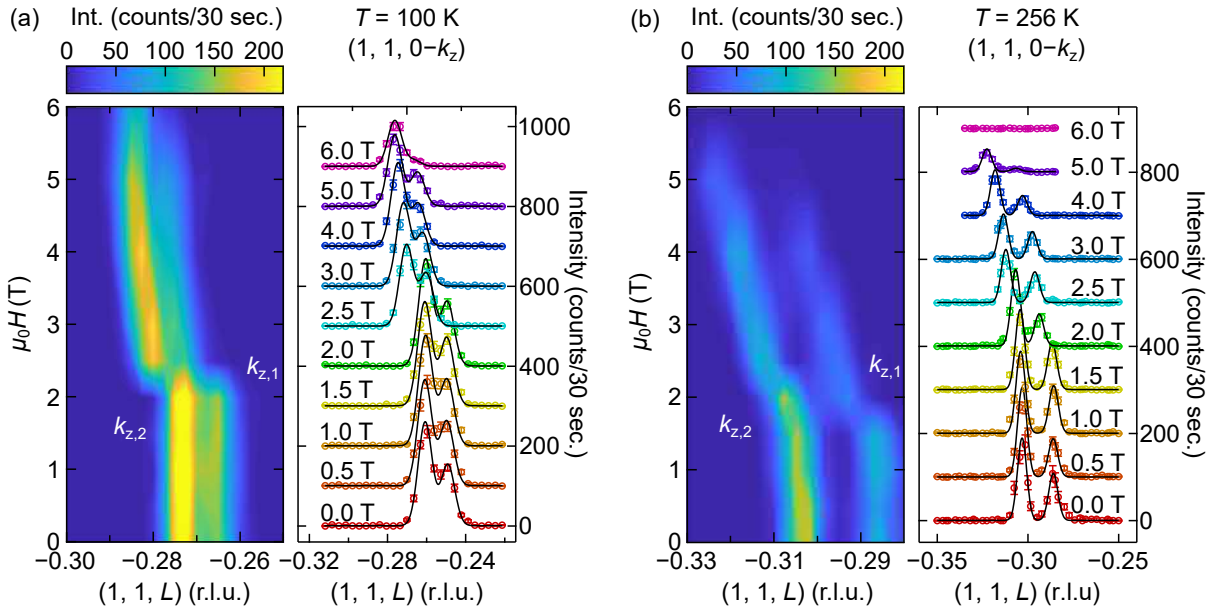

FIG. S3 : Temperature and magnetic field dependence of incommensurate magnetic Bragg peaks (1, 1, $0 - k_z$). a) The evolution of Bragg peaks $k_{z,1}$ and $k_{z,2}$ with an applied magnetic field at 100 K and b) 256 K. For both (a) and (b), the solid black lines in the right-hand panels are Gaussian fits to the data as described in the text. An offset of 100 counts/30 sec. was added between individual L scans for clarity.

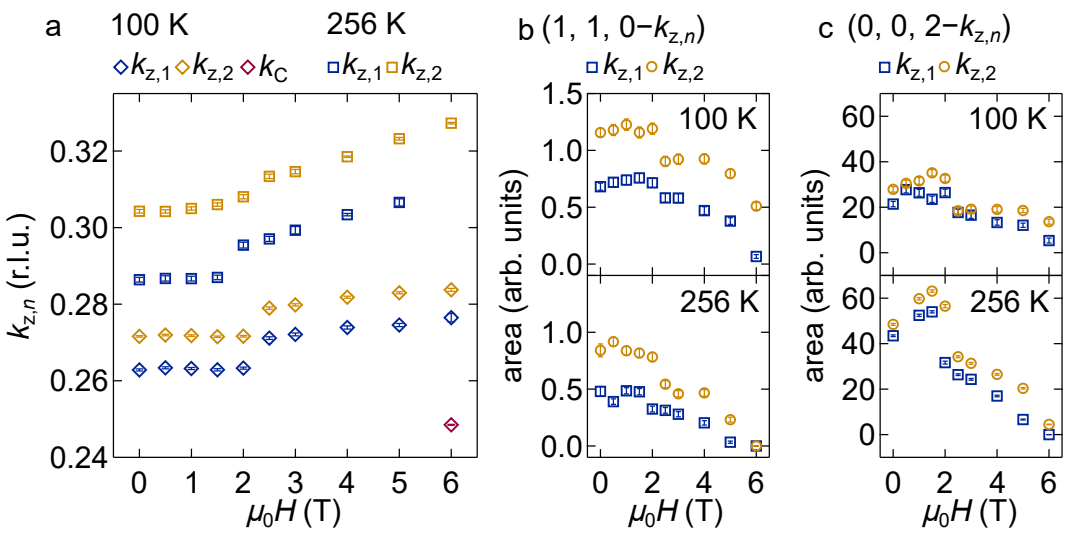

FIG. S4 : Temperature and magnetic field dependence of wave vector and intensity of incommensurate magnetic Bragg peaks. a) The evolution of wave vectors (0, 0, $k_{z,1}$) and (0, 0, $k_{z,2}$) depicted in Fig. 3(a) of the main text with applied magnetic field at 100 K and 256 K. An additional commensurate peak, $k_c = 0.25$, appears at 6 T in the 100 K data. b) Integrated intensity of the Bragg peaks (1, 1, $0 - k_{z,n}$) depicted in Fig. S3 at 100 K and 256 K. c) Integrated intensity of Bragg peaks (0, 0, $2 - k_{z,n}$) depicted in Figs. 3(b) and (c) of the main text as a function of magnetic field applied along [1, $\bar{1}$, 0].

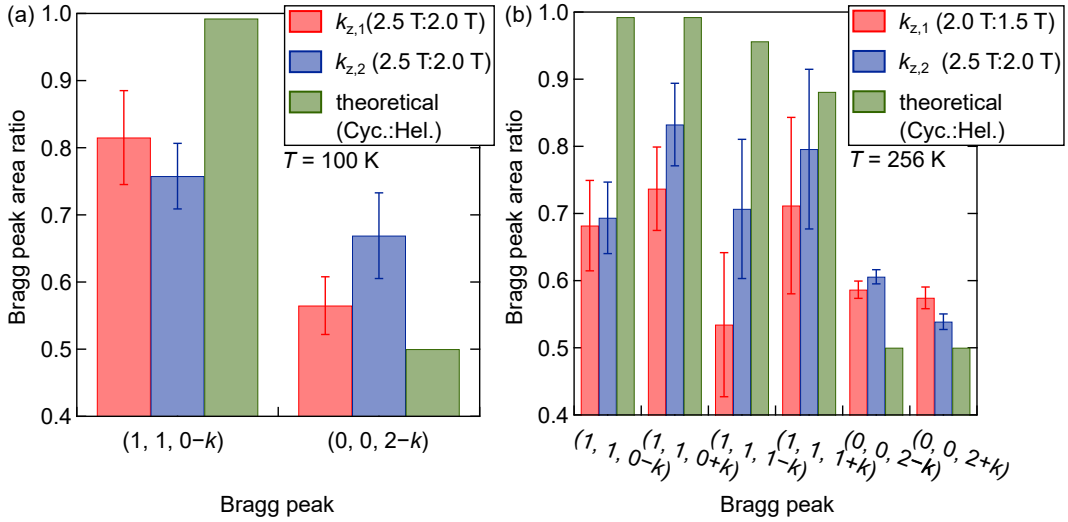

FIG. S5 : Comparison of cycloidal vs helical spiral intensity. Ratio of intensities just above H_1 to just below H_1 for the incommensurate Bragg peaks measured at (a) 100 K and (b) 256 K. The calculated values of the cycloidal:helical magnetic structure factor ratios are shown in green for comparison.

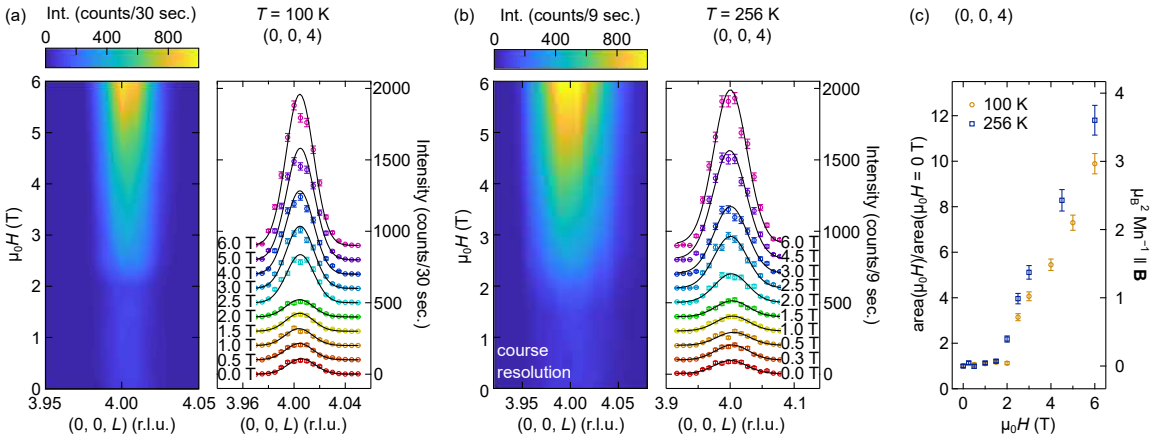

FIG. S6 : Nuclear Bragg peak intensity as a function of magnetic field. (0, 0, 4) Bragg peak intensity tracked at (a) 100 K and (b) 256 K as a function of applied magnetic field applied along $[1, \bar{1}, 0]$ crystallographic axis. The increase in intensity as the field increases is indicative of a net component of magnetization emerging due to the moments canting towards the applied field direction. The solid lines in the righthand panels of (a) and (b) are the Gaussian fits to the data described in the text. An offset was added between individual L scans for clarity (offsets are 100 counts/30 sec. for (a) and 100 counts/9 sec. for (b)). Panel (c) shows the intensity versus H, divided by the intensity at $H = 0$ where only the nuclear structure contributes intensity. The right hand axis displays the projection of the moment, in $\mu_B^2 \mathrm{Mn}^{-1}$, along the applied field direction.

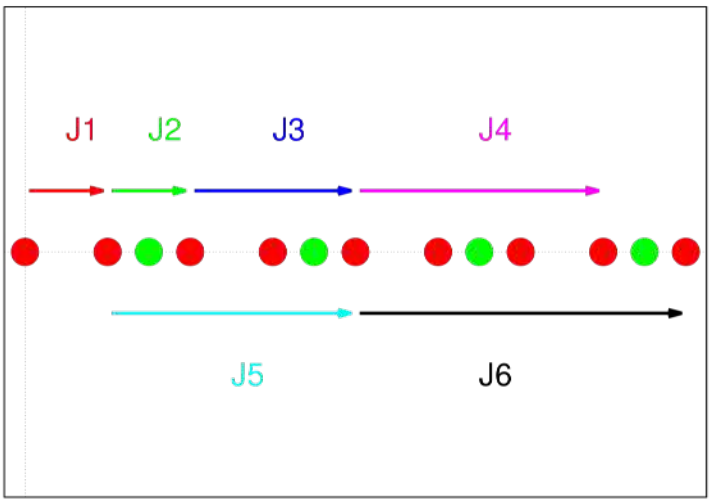

FIG. S7 : Schematic of exchange interactions along c-axis. First 6 exchange interactions between Mn layers. Red: Mn layer; green: spacer layer including Y [see Fig.1(a) of the main text].

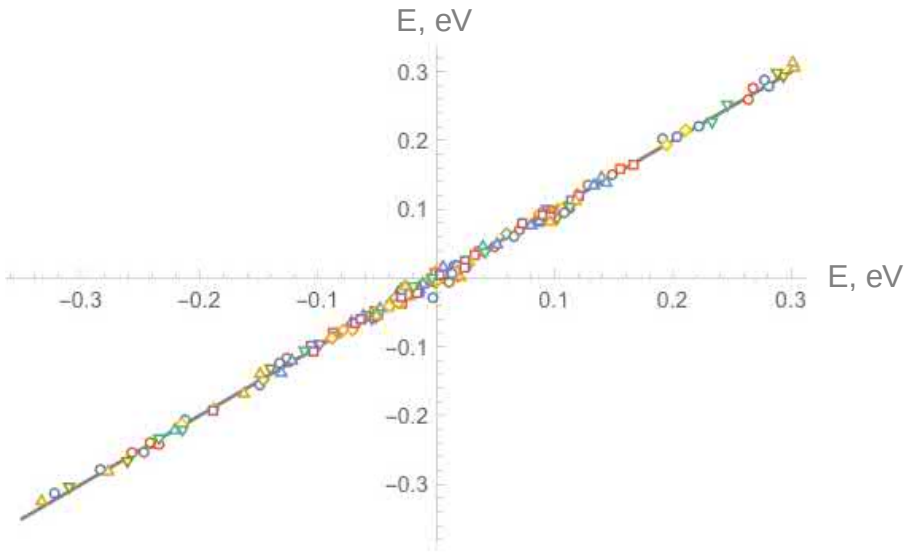

FIG. S8 : Fitted vs. calculated values of total energies. Blue circles are the calculated values for $U - J = 0$. Other symbols are for other values of U. Deviations from the straight line indicate fitting errors.

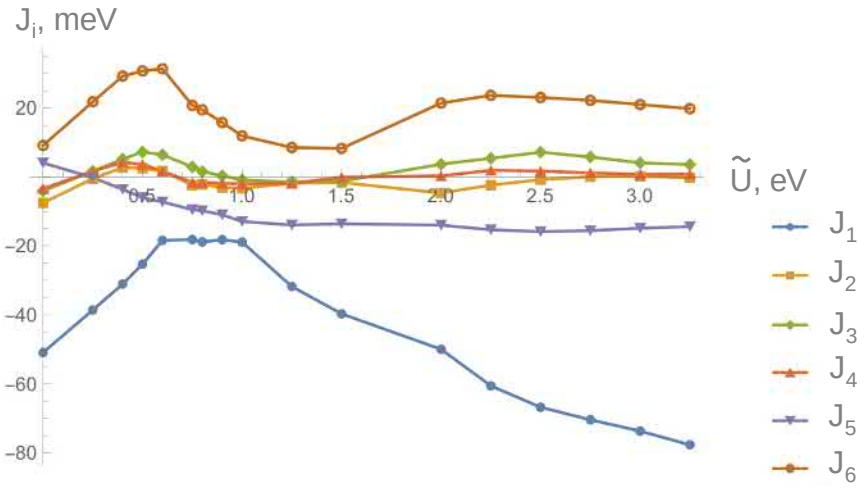

FIG. S9 : Fitted values of the exchange constants. Fitted values of the exchange constants J_1–J_6 as a function of $\tilde{U} = U - J$.

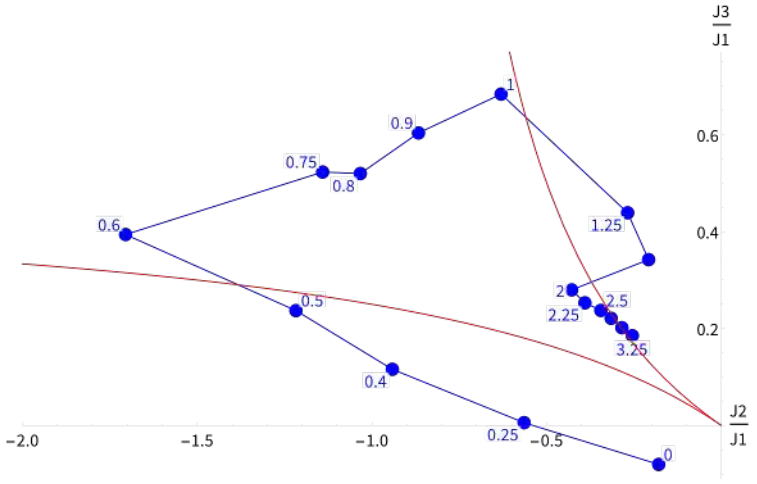

FIG. S10 : Calculated phase diagram. Phase diagram of the $J_1 - J_2 - J_3$ model in the $J_2/J_1 - J_3/J_1$ coordinates. The region between the two red lines is a spiral state, above them is the FM, and below the AF *uudd* state. The points reflect the calculated values of J_1, J_2, J_3 for different values of $U - J$.

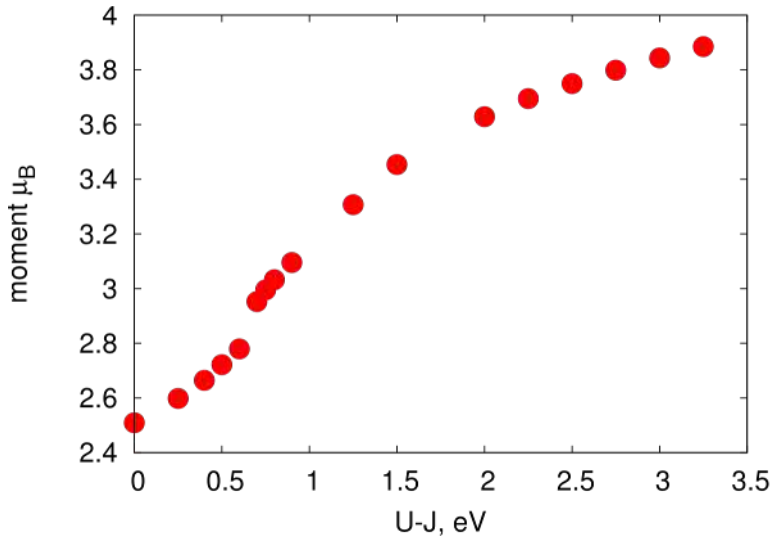

FIG. S11 : Calculated magnetic moments. Calculated magnetic moments on Mn (square-averaged over all 8 sites and all 10 configurations) as a function of $U - J$.

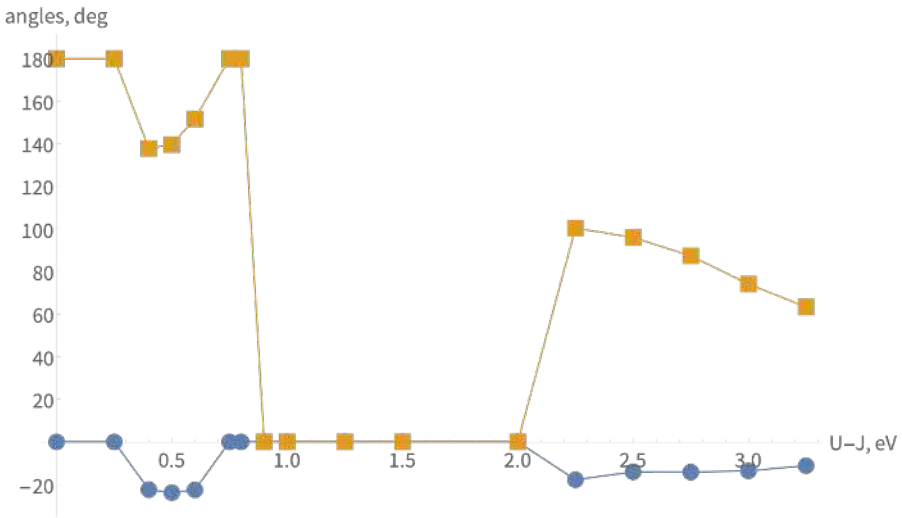

FIG. S12 : Calculated spiral angles. Calculated spiral angles $\boldsymbol{\alpha}$ and $\boldsymbol{\beta}$ (see the text for the definitions).

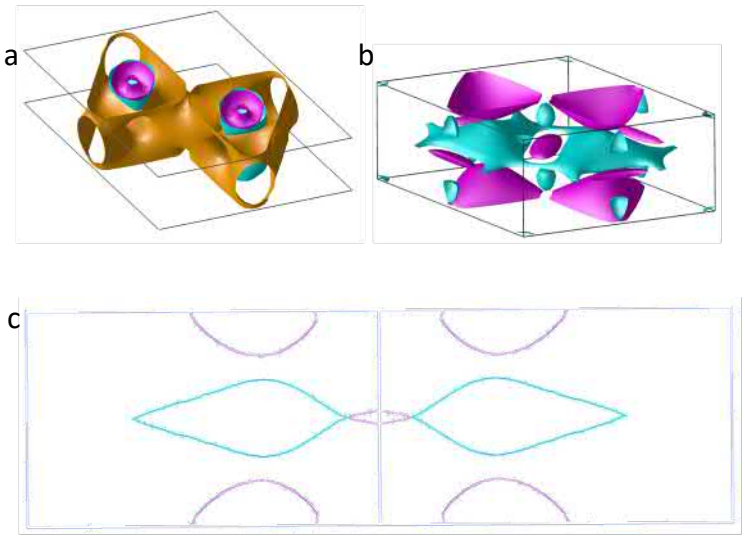

FIG. S13 : Calculated Fermi surface. Fermi surface calculated without Hubbard U for the ferromagnetic ordering a) spin-minority, and b) spin-majority electrons. c) A vertical cut of the spin-majority Fermi surface in the Γ-K-K-A plane.

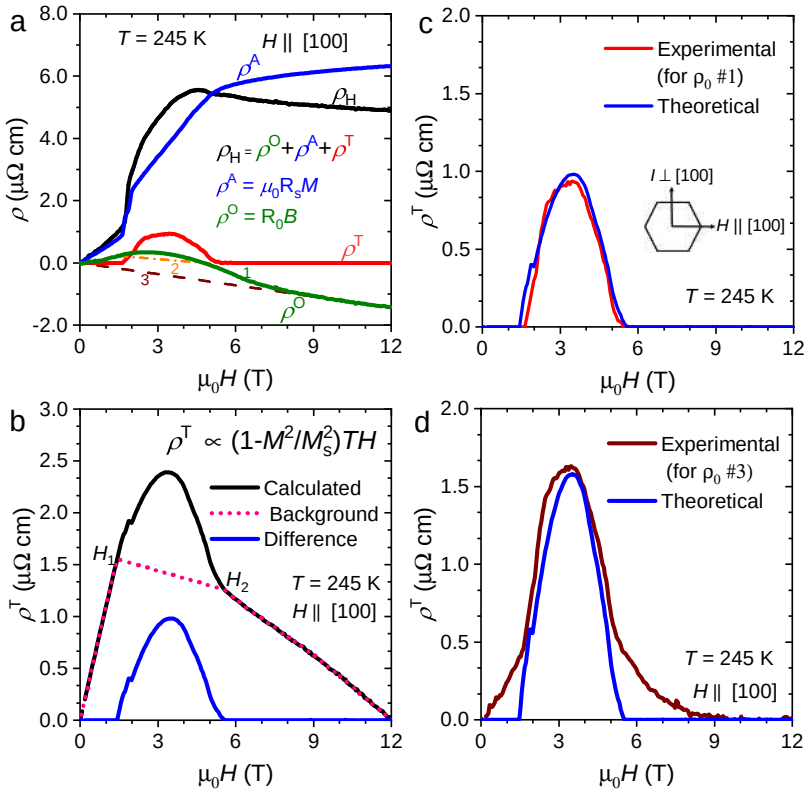

FIG. S14 : Estimation of topological Hall resistivity at 245 K from measured data and theoretical model. a) Hall resistivity and its various components. Three different ρ^0 are labelled as 1, 2 and 3 and are discussed in the text in S6. b) Topological Hall effect calculated using the chiral spin texture model discussed in S5. Since there is no THE outside of TCS phase, the component obtained outside this phase is subtracted as a background (pink dashed line) from the calculation carried out in the entire field range (black solid line) from 0 to 12 T to obtain the THE (blue solid line) in the TCS phase. c) Topological Hall resistivity estimated using ρ^0 labelled as 1 in panel (a) compared to that obtained form the theoretical model. d) Topological Hall resistivity estimated using ρ^0 labelled as 3 in panel (a) compared to that obtained form the theoretical model. Results presented in panels (c) and (d) show that the theoretical model describes the experimental data well irrespective of the method used to estimate the ordinary component of the Hall resistivity (ρ^0). The theoretical model is the plot of Eq. S35 (or Eq. 2). The arrows in the hexagon in (c) indicate the field and current directions in the hexagonal lattice of YMn_6Sn_6.

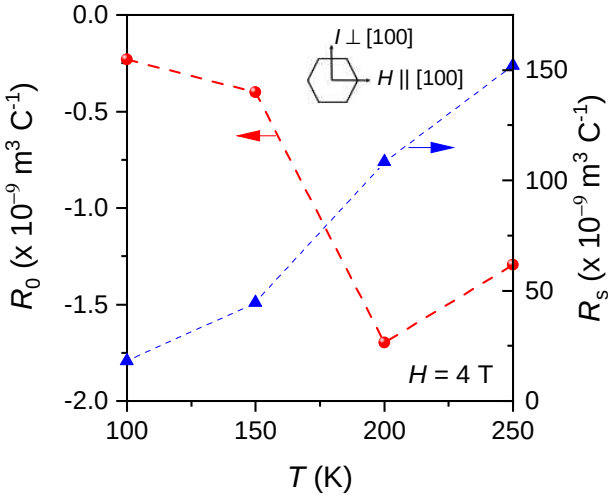

FIG. S15 : Temperature dependence of coefficients of normal and anomalous Hall resistivity. Temperature dependence of coefficient of normal Hall resistivity (R_0), and anomalous Hall resistivity (R_s) derived from ρ_H and used to estimate the temperature dependance of ρ^T depicted in Fig. 4(d). The arrows in the hexagon indicate the field and current directions in the hexagonal lattice of YMn_6Sn_6.

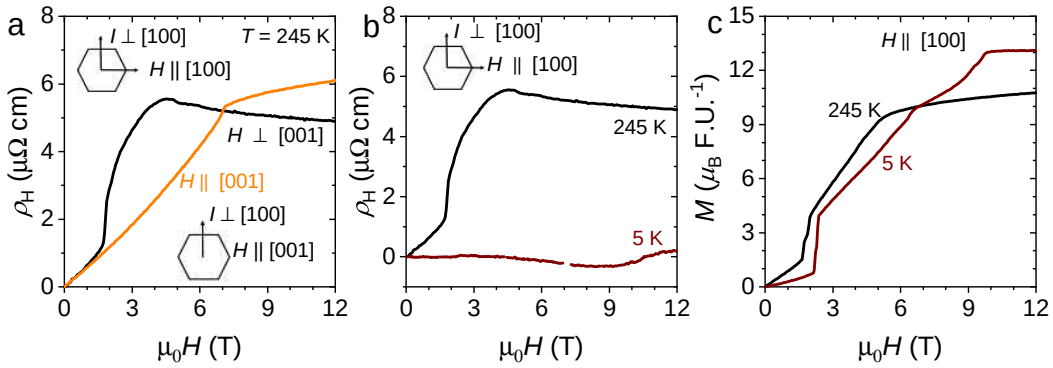

FIG. S16 : Hall resistivity and magnetization of YMn_6Sn_6. a) Hall resistivity at 245 K measured with magnetic field in the *ab*-plane and along the *c*-axis. The current was applied along the same direction in these two measurements carried out on two different samples. b) Hall resistivity at 5 K and 245 K measured with magnetic field applied in the *ab*-plane. c) Magnetization at 5 K and 245 K measured with the magnetic field in the *ab*-plane. The arrows in the hexagon in (a) and (b) indicate the field and current directions in the hexagonal lattice of YMn_6Sn_6.

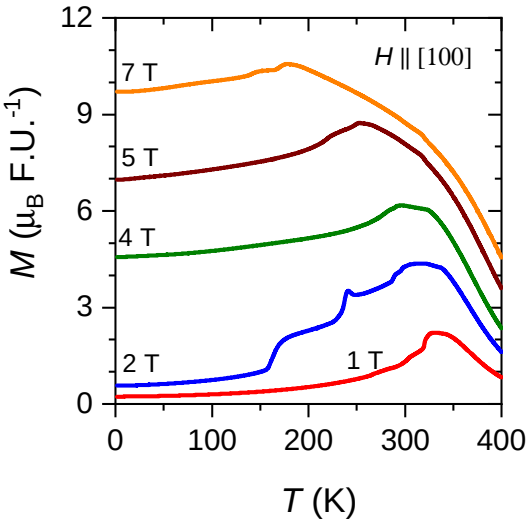

FIG. S17 : Magnetic moment of YMn_6Sn_6 as a function of temperature. Magnetic moment as a function of temperature at indicated magnetic fields applied in the *ab*-plane. Above 3 T and below 250 K, magnetic moment changes very little with the temperature.